Global assessment of terrestrial water cycle resilience

Romi A. Lotcheris[1,2*], Nielja S. Knecht[1,2], Lan Wang-Erlandsson[1,2,3], Juan C. Rocha[1,2*]

[1*]Stockholm Resilience Centre, Stockholm University, Stockholm, SE-106 91, Sweden.
[2]Bolin Centre for Climate Research, Stockholm University, Stockholm, 10587, Sweden.
[3]Potsdam Institute for Climate Impact Research, Member of the Leibnitz Associations, Potsdam, 14473, Germany.

*Corresponding author(s). E-mail(s): romi.lotcheris@su.se; juan.rocha@su.se;

Abstract

Green water - transpiration, soil moisture, and land precipitation - is critical for Earth system stability and ecosystem productivity. Despite evidence of considerable and widespread change globally, its resilience, or ability to absorb and recover from disturbances, is not yet well understood. Here, we assess green water resilience using early warning signals (EWS) applied to global satellite time series of green water variables, and empirically evaluate these estimates against past abrupt changes. We find that a wider portfolio of context-appropriate EWS are needed to capture heterogeneous water–vegetation dynamics across eco-hydrological systems, and show that EWS provide limited but non-negligible additional skill in anticipating abrupt transitions when combined with environmental context. We find ecosystem-dependent signatures of resilience loss globally, with drylands and grasslands showing widespread critical slowing down, and high-latitude systems showing critical speeding up and flickering behaviour, highlighting emerging risks to green water dynamics under ongoing anthropogenic pressures.

Keywords: Green water, Terrestrial water cycle, Resilience, Early warning signals

1 Introduction

Water plays a crucial role in regulating the functioning and stability of the Earth system [1–3]. Yet, research points to widespread anthropogenic pressures on the terrestrial water cycle [3–5]. Green water - the water which is available to and used by vegetation - is critical for maintaining hydro-ecological and hydro-climatic Earth system functions [1, 2, 6], mediating soil–water–vegetation interactions that generate critical feedbacks for ecosystem and climate functioning. These feedbacks depend strongly on hydro-ecological context. For example, in energy-limited tropical forests, transpiration is closely linked to moisture recycling dynamics that are affected by land cover change [7, 8], whereas in water-limited ecosystems, soil moisture-vegetation feedbacks play a more important role [9, 10]. Through these feedbacks, changes to green water variables can have self-amplifying, non-linear effects [3].

Given the potential for these feedbacks to generate non-linear changes in the water cycle and vegetation dynamics, understanding green water resilience is critical for assessing how human pressures are altering the water cycle. Resilience describes a system's ability to absorb disturbances, reorganize, and maintain its essential structure and functions [11–13]. As a system loses resilience, it becomes vulnerable to abrupt transitions from one qualitative regime to another [14]. Early warning signals (EWS) have been used as statistical proxies for resilience. Often based on measured changes to autocorrelation and variance [12, 15], EWS have been used to assess resilience in terrestrial ecosystems, applied to gross primary productivity and leaf area index [16], normalized difference vegetation index [17–19], or vegetation optical depth [17, 20]. Despite the close coupling of green water variables to terrestrial ecosystems, water is typically treated as a static explanatory driver, thereby not accounting for changes in the water cycle dynamics that both drive and respond to changes in vegetation. As a result, the resilience of green water variables themselves is not yet well understood. Additionally, ground-truth validation of vegetation resilience assessments has been done in only a few documented, often local cases (see ref. [21]). A validation of green water resilience indicators against ground-truth observations has not yet been undertaken.

Here, we aim to understand the resilience of green water variables, globally, and develop methods to validate the performance of resilience loss assessments. We do this by applying EWS to satellite derived time series of transpiration, surface soil moisture, and precipitation over land. We expand resilience assessments from ecosystem states to include key drivers related to the water cycle, and further present an approach to validate EWS against an empirically determined ground-truth of abrupt shifts in green water dynamics.

2 Main

We analyse four phenomena of resilience loss: critical slowing down (CSD), critical speeding up (CSU), flickering, and the fractal dimension. These are measured by five rolling-window indicators computed from each green water time series: lag-1 autocorrelation (AC1), standard deviation (SD), skewness, kurtosis, and fractal dimension (FD) (Table 1). We do this to account for multiple pathways through which a forcing can alter green water dynamics (Section 4.2). The direction and strength of change in each indicator are quantified using Kendall's τ. Importantly, we treat both positive and negative τ as potentially informative, given that multiple drivers [22], changing noise regimes, and stochasticity [23], mean that gradual increases in AC1 and variance alone may be difficult to observe [13, 24, 25].

To assess the accuracy and uncertainty of EWS, we construct an empirical ground truth by applying a breakpoint detection method to each pixel-wise time series of transpiration, soil moisture, and precipitation [26]. We approximate a hydrological transition as a quantitative shift in the residuals of a time series, thereby determining a set of true positives (time series with at least one breakpoint) and true negatives (time

Table 1 Early-warning signals (EWS) used in this study, the indicators used for each EWS and their typical signs, and their interpretation. Indicators are computed in 5-year rolling windows and summarised by Kendall's τ trend statistic.

EWS	**Indicator**	**Shorthand**	**Interpretation**
Critical Slowing Down (CSD)	↑ Lag-1 autocorrelation	AC1 (τ_{AC1})	Trend in short-term persistence
	↑ Standard deviation	SD (τ_{SD})	Trend in variability
Increased tendency for system states to be distributed further from equilibrium and slower to recover. A wider and shallower basin of attraction reduces resilience			
Critical Speeding Up (CSU)	↓ Lag-1 autocorrelation	AC1 (τ_{AC1})	Trend in short-term persistence
	↓ Standard deviation	SD (τ_{SD})	Trend in variability
Narrowing of the basin of attraction increases the likelihood of exiting the basin. Resilience reduced by increasing vulnerability to stochastic transitions.			
Flickering	↑↓ Skewness	Skew (τ_{Skew})	Trend in asymmetry
	↑ Kurtosis	Kurt (τ_{Kurt})	Trend in tail-heaviness
Increasing tendency for system states to exist at distribution tails (i.e., more frequent/extreme excursions).			
Fractal dimension	↓ Fractal dimension	FD (τ_{FD})	Trend in temporal structure & long-term memory
Scale-free measure of temporal memory of a time series. Increasing self-similarity and slower recovery reduces resilience.			

series without detected breakpoints) (Section 4.3). We use these in a machine-learning framework to evaluate how well EWS anticipate changes in green water variables, and understand which indicators and directions are informative (Section 4.4).

We apply this approach to precipitation, transpiration, and soil moisture, representing the input, storage, and release of water available to terrestrial vegetation. Because the three variables are derived from distinct satellite products with differing noise characteristics, uncertainties, and spatial coverage, we estimate EWS and interpret results separately for each variable.

2.1 Abrupt shifts in green water are coherent in time and space

We detect abrupt shifts in all three green water variables, with pronounced spatial and temporal coherence in breakpoint timing (Fig. 6). Neighbouring pixels frequently shift in the same years, indicating synchronous changes across larger land areas. The affected land area also accumulates over time. Between 2000 and 2020, 22.6% of land between 60°S and 60°N has experienced an abrupt shift in precipitation, 7.5% in transpiration, and 3.5% of land area excluding dense tropical forests has experienced abrupt shifts in soil moisture (Supplementary Fig. 7).

Transpiration. Abrupt shifts are generally detected in the northern high-latitudes, South America, Central Asia, and Australia, with almost none detected in temperate ecosystems (Fig. 6a). Abrupt shifts in the high-latitudes are associated with an increase in transpiration, whereas shifts South America, Central Asia, and Australia are generally associated with a decrease. In the tropics, high absolute differences, and lower proportional change is likely the result of higher baseline transpiration. The opposite effect occurs in drier regions, where higher absolute differences also lead to greater proportional changes (Fig. 6b). We also find an increase in transpiration in the Sahel region following abrupt shifts, with breakpoints detected in the 2010s.

Soil moisture. Abrupt shifts are more common in more arid regions, with a smaller absolute decrease in soil moisture following an abrupt shift compared to transpiration and precipitation (Figure 6a and b). Large parts of Argentina and southern Brazil show shifts in the early 2000s, which are followed by substantial proportional declines in soil moisture. Adjacent regions show shifts in the later 2000s and 2010s. Southern Africa, western Australia, and northern Mexico show similar patterns. Shifts associated with increases in soil moisture are detected in the Sahel region, progressing northwards in later years. We also detect increasing soil moisture following abrupt shifts in Eastern China and Eastern Australia.

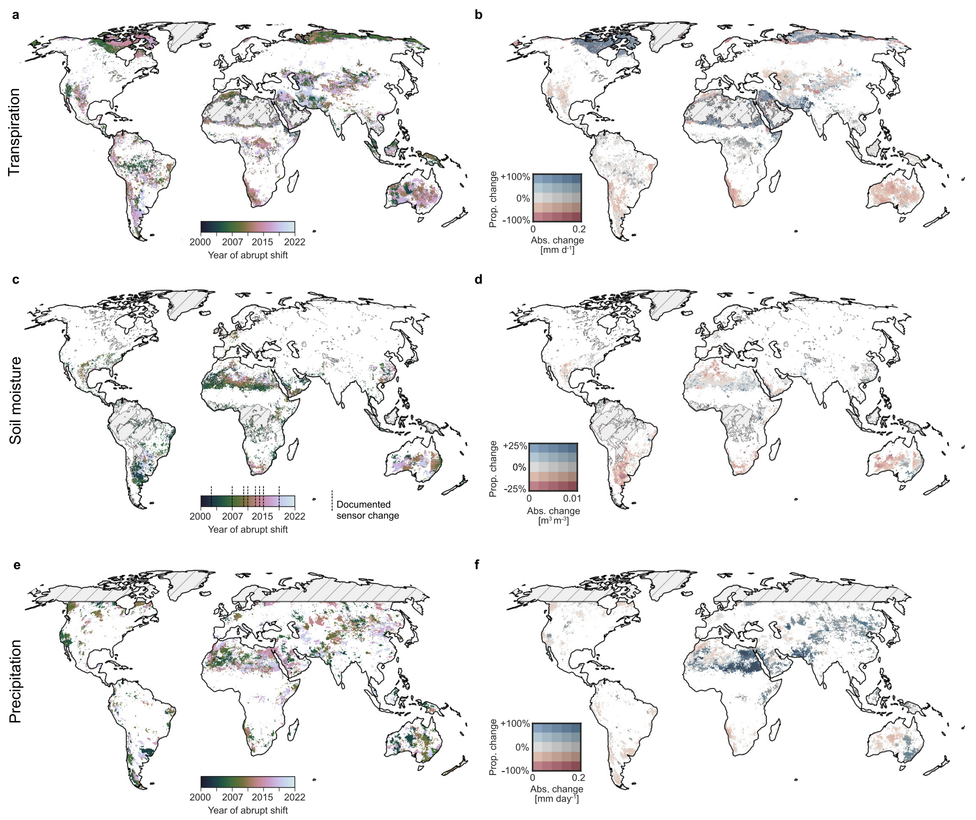

Fig. 1 Spatial patterns of abrupt shift in mean for green water variables. Year of first detected significant breakpoint from the structural change test ($p < 0.05$), and the proportional and absolute difference between the mean before and after the detected breakpoint in transpiration (a - b), soil moisture (c - d) and precipitation (e - f). The proportion of change is calculated by dividing the mean after the breakpoint by the mean before the breakpoint. Darker colours indicate both a high proportional change and a high absolute difference in mean before and after the breakpoint. Lighter colours indicate a high proportional change, but a low absolute difference. No data is given by a grey hatch.

Precipitation. Abrupt shifts are concentrated in the mid-latitudes (approximately between 30°N and 30°S), with no shifts detected in humid equatorial regions. Shifts associated with an increase in precipitation are concentrated in central and eastern Asia and northern Africa, while those associated with a decrease are found in South America, southern Africa, and Australia (Figure 6c). We detect fewer shifts in South America compared to soil moisture and transpiration, while southern Africa

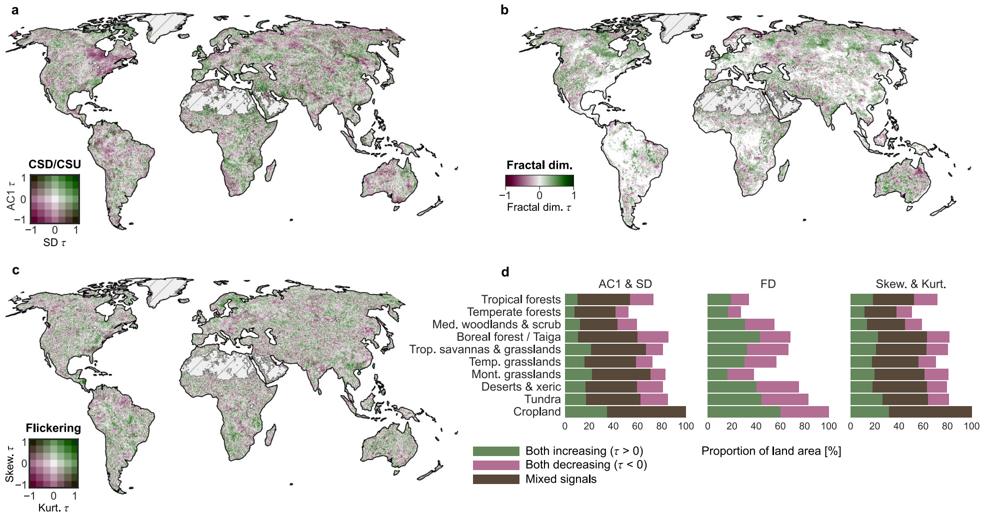

Fig. 2 Spatial patterns of early warning signals (EWS) for transpiration. Panels (a - c): (a) Spatial patterns of changes to autocorrelation (AC1) and standard deviation (SD), related to critical slowing down (CSD) and critical speeding up (CSU); (b) Spatial patterns of changes to the fractal dimension, where decreasing FD is the EWS; (c) Spatial patterns of changes to skewness and kurtosis, related to flickering. Green shading denotes pixels where both metrics are simultaneously increasing, pink shading denotes pixels where both are decreasing; brown shading denotes pixels where one metric increases while the other decreases. White regions did not exhibit statistically significant trends in the respective metrics, grey hatch indicates regions with missing data. All trends were assessed via Kendall's τ ($p < 0.05$). Bar plots show the proportion of land area for each EWS where indicators are simultaneously increasing, decreasing, or showing mixed signals.

shows synchronous shifts around the 2010s. Both regions experienced abrupt declines in precipitation.

2.2 Resilience loss in green water globally

Signals of resilience loss in the terrestrial water cycle occurred across all biome types (Figs. 2–4). Spatial patterns are largely heterogenous, but some regional patterns emerge, which differ across green water variables (transpiration, soil moisture, precipitation) and EWS types (Section 4.2). CSD is more frequent in water-limited systems, especially grasslands and drylands, while higher-latitude ecosystems show more flickering and CSU. Tropical and temperate grassland biomes consistently exhibit higher proportions of EWS across variables, particularly signals of CSD and FD.

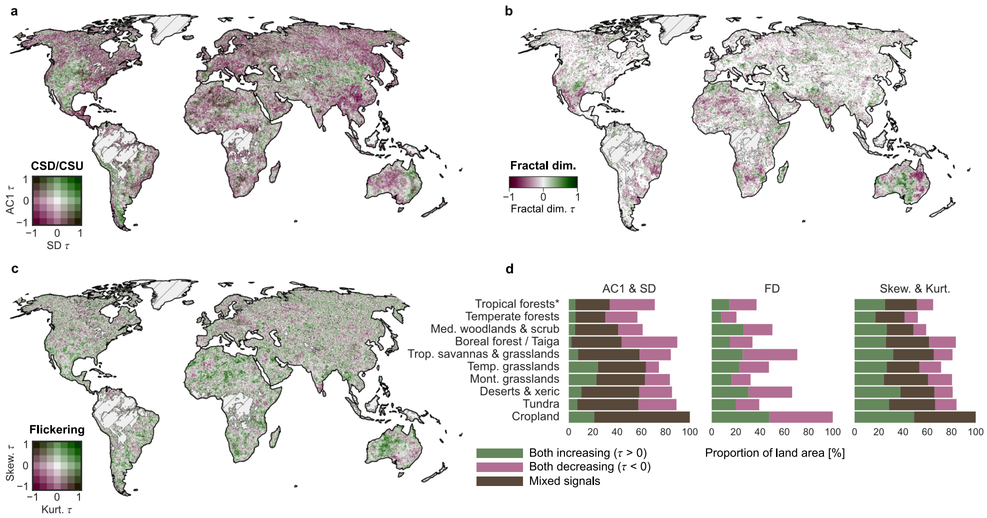

Fig. 3 Spatial patterns of early warning signals (EWS) for soil moisture. Panels (a - c): (a) Spatial patterns of changes to autocorrelation (AC1) and standard deviation (SD), related to critical slowing down (CSD) and critical speeding up (CSU); (b) Spatial patterns of changes to the fractal dimension (FD), where decreasing FD is the EWS; (c) Spatial patterns of changes to skewness and kurtosis, related to flickering. Green shading denotes pixels where both metrics are simultaneously increasing, pink shading denotes pixels where both are decreasing; brown shading denotes pixels where one metric increases while the other decreases. White regions did not exhibit statistically significant trends in the respective metrics, grey hatch indicates regions with missing data. All trends were assessed via Kendall's τ ($p < 0.05$). Asterisk marks biomes where satellite coverage of soil moisture is incomplete; proportions reflect only pixels within the biome where data was available.

Transpiration. While mixed AC1–SD signals dominate across biomes (Figure 2a), CSD signals show prominent clusters in dryland and savanna regions in southern South America, the Miombo woodlands in Southern Africa, the Sahel, and north-eastern Australia (Fig. 2a and d). CSU signals are most prevalent in boreal forests, tundra, and deserts. FD decreases in tundra, deserts, tropical grasslands, and temperate grasslands biomes (Fig. 2d). Flickering is most frequent in mid- to high latitudes, with high proportions in tundra and boreal forests, but also tropical savannas, including Brazil (Fig. 2c).

Soil moisture. CSD-based EWS are less frequent, also dominated by mixed AC1–SD signals (Fig. 3a). Some CSD clusters were present in southern North America, the Andes and southern Argentina, north-eastern Australia, and central Asia, with

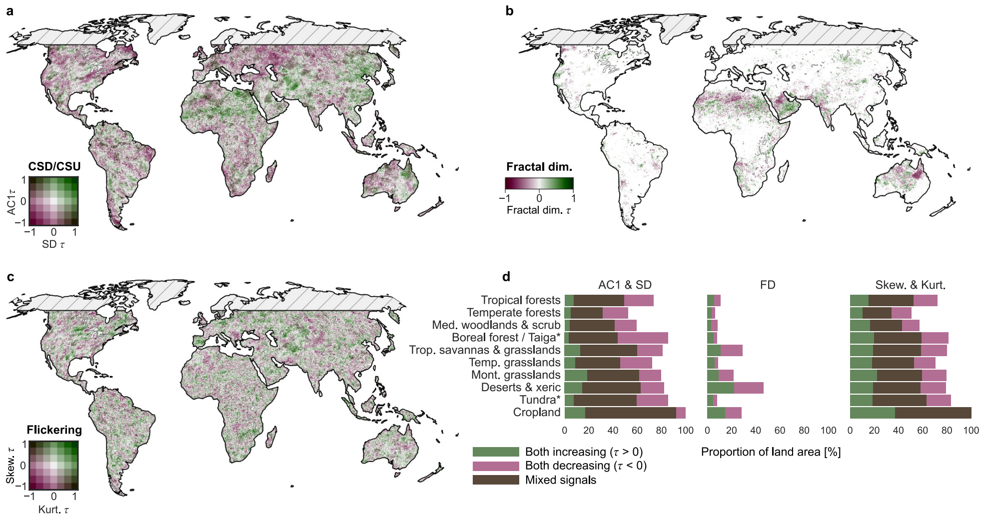

Fig. 4 Spatial patterns of early warning signals (EWS) for precipitation. Panels (a - c): (a) Spatial patterns of changes to autocorrelation (AC1) and standard deviation (SD), related to critical slowing down (CSD) and critical speeding up (CSU); (b) Spatial patterns of changes to the fractal dimension, where decreasing FD is the EWS; (c) Spatial patterns of changes to skewness and kurtosis, related to flickering. Green shading denotes pixels where both metrics are simultaneously increasing, pink shading denotes pixels where both are decreasing; brown shading denotes pixels where one metric increases while the other decreases. White regions did not exhibit statistically significant trends in the respective metrics, grey hatch indicates regions with missing data. All trends were assessed via Kendall's τ ($p < 0.05$). Bar plots show the proportion of land area. Asterisk marks biomes where satellite coverage of precipitation is incomplete; proportions reflect only pixels within the biome where data was available.

highest proportions in temperate and montane grasslands (Fig. 3d). Spatial overlap between soil moisture and transpiration CSD occurs in parts of Argentina, southern Brazil, and central Mexico (Figs. 2a and 3a). CSU signals in soil moisture are most frequent in boreal forests and tundras. FD decreases in subtropical and dryland regions, tropical grasslands, deserts, as well as temperate grasslands and Mediterranean forests (Fig. 3b). Flickering signals were heterogenous, with less clear spatial patterns.

Precipitation. Mixed AC1–SD signals dominated across biomes (Fig. 4a). CSD was most prevalent in subtropical and arid regions, with deserts and tropical grasslands showing the highest proportions. CSU signals were more common in temperate grasslands and forests, and in tropical savannas (Fig. 4d). Tropical forests, which show few CSD signals, exhibit relatively more CSU for both transpiration and precipitation. FD decreases in precipitation are rare compared to transpiration and soil moisture but, where present, are concentrated in subtropical drylands, especially deserts and tropical savannas (Fig. 4b). Flickering patterns are heterogeneous, with highest proportions in montane and tropical grasslands (Fig. 4c).

Our results are robust across different methods to assess the direction and significance of the EWS (Supplementary Fig. 6). While sensitive to the rolling window length and temporal aggregation, we find that a 5-year rolling window at weekly timescales best balances noise and excessive dampening of longer windows (section 4.5; Supplementary Table 1).

2.3 Performance and EWS are context dependent

To understand under which conditions early-warning signals (EWS) can anticipate abrupt shifts in green water dynamics, we use a machine learning framework (Section 4.4) to test how much both EWS and environmental variables contribute to predicting detected abrupt shifts (Section 2.1). We use Shapley (SHAP) values, reported as log-odds, to quantify the marginal contribution of EWS and environmental variables to predicting abrupt shifts that occurred at least 12 years after the start of the time series. EWS predictors are computed only from observations prior to the detected shift; environmental predictors summarise conditions over the full time series. Positive SHAP values indicate that explanatory variables raise the probability of detecting a True abrupt shift, whereas negative values indicate higher chances of False shifts. We find EWS make only a modest contribution to model skill; most predictive power comes from environmental context. However, the relative importance of EWS compared to environmental variables differs across hydro-ecological system types and green water variables (Fig. 5).

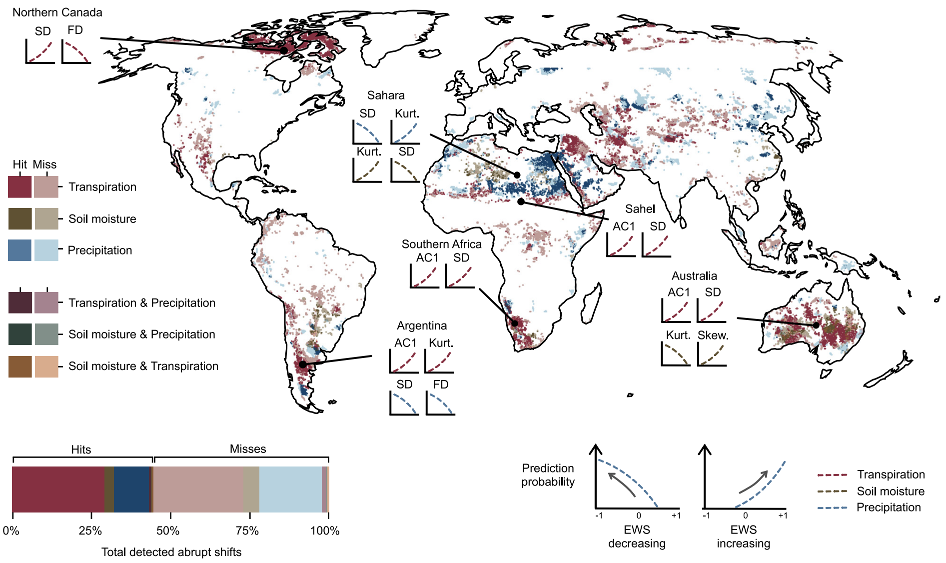

Fig. 5 Different regions and green water variables are characterised by different EWS τ as the strongest predictors of abrupt shifts. For transpiration, soil moisture, precipitation, and their combinations, regional summaries list the two most influential EWS τ (SHAP-ranked) and the sign associated with increased predicted probability of an abrupt shift; both increasing and decreasing EWS τ can be associated with higher risk, illustrated in the bottom right schematic. Spatial shading indicates hits (darker) and misses (lighter). The bottom bar plot summarises their respective proportions for the green water variables and their combinations.

Transpiration. Models achieve the highest skill for transpiration (PR AUC = 0.49 versus baseline 0.06; Supplementary Table 10). Environmental variables account for most of this skill, with EWS adding some complementary information. Gross primary productivity variance, autocorrelation (τ_{AC1}), transpiration variance, and PET variance are dominant predictors (Fig. A1a). Correctly predicted shifts cluster in Northern Canada, southern South America, Southern Africa, the Sahel, and Australia (Figure 5). In these regions, most influential EWS combinations typically involved increasing τ_{AC1} and τ_{SD}, which are associated with higher predicted probability of an abrupt shift. This is consistent with CSD in dryland and transition zones (Section 2.2). Missed shifts, together with regional SHAP summaries, suggest that EWS for transpiration have limited predictive value in humid tropical forests and some temperate regions (Fig. A1).

Soil moisture. Models achieve only modest skill (PR AUC ≈ 0.21 versus baseline 0.02; Supplementary Table 10). Abrupt shifts are rarer and spatially isolated, and environmental and climatic variables dominate model performance. Mean temperature, soil moisture variance, temperature variance, temperature trend, and PET variance are dominant predictors (Fig. A1b). Detected soil moisture shifts occur mainly in parts of Australia and the Sahara, where combinations of τ_{Kurt}, τ_{Skew}, and τ_{SD} were important (Fig. 5). However, EWS τ do not exhibit clear, consistent associations with increased predicted probability (Fig. A2b), indicating that the indicators used here provide little systematically predictive information for soil moisture at the global scale.

Precipitation. Model performance for precipitation is intermediate (PR AUC = 0.33 versus baseline 0.05; Supplementary Table 10). Environmental drivers again explain most predictive power (Drivers-only PR AUC = 0.24; EWS-only PR AUC = 0.06), but EWS add complementary information in the full model (PR AUC = 0.33) τ_{Kurt}, τ_{SD}, temperature variance, mean precipitation were are dominant environmental predictors (Fig. A1c). Correctly predicted abrupt shifts in precipitation are concentrated along dryland boundaries, including Egypt and regions north of the Sahel, with additional clusters in Argentina and parts of south-eastern Russia and China (Fig. 5). In Argentina, decreasing τ_{SD} and τ_{FD} are associated with higher predicted probability, whereas in the Sahara and northern Sahel decreasing τ_{SD} and increasing τ_{Kurt} is influential. These patterns are consistent with critical speeding up of precipitation in drier margins of humid systems (Section 2.2). Increasing kurtosis, and decreasing SD and FD τ show linear associations with increased predicted probability (Fig. A2), consistent with CSU-like signals having some predictive value, particularly for more humid systems (Fig. A1).

3 Discussion

We find ecosystem-dependent signatures of resilience loss in green water variables. For transpiration, we find that increasing AC1 and SD provide predictive power in estimating abrupt shifts. Signals of CSD (simultaneously increasing AC1 and variance) and decreasing FD were most pronounced in drylands and transitional systems, consistent with evidence of lower resilience with increasing aridity [27], and with research identifying the regions such as the Caatinga, prairies, and grasslands of North America and Asia as sensitive to water availability [28]. Regions where we detect CSD in transpiration and soil moisture overlap with regions identified as at risk of abrupt aridification [10, 29, 30]. Crucially, signals of resilience loss in drylands, grasslands, and tropical forests point towards potential risks to green water functions that may disproportionately affect communities in the Global South.

For precipitation, decreases in SD and FD and increases in kurtosis were associated with a higher probability of detecting an abrupt shift. Previous studies in the Amazon have reported increasing AC1 and variance in vegetation, interpreting decreasing AC1 and variance in wetter regions as resilience gain [17, 20, 31]. We do not detect widespread CSD-like EWS in Amazon precipitation, suggesting that observed vegetation resilience loss is unlikely to be explained solely by CSD in a precipitation driver [15], and may instead be consistent with resilience loss in vegetation. We find that CSU-like signals in precipitation are associated with an increased probability of abrupt shifts, particularly in drier, water-limited regions such as savannas and temperate grasslands.

In boreal forest and tundra biomes, signals of CSU were prevalent across all green water variables. In these regions, rapid warming has led to permafrost thaw and improved soil drainage [32], earlier snow melt [33], and vegetation reorganisation, for example an increase in deciduous vegetation in boreal forests with changes in phenology and a faster growing period and shrub encroachment in the tundra [34, 35].

The effects these changes have on soil moisture and vegetation may contribute to CSU signals in transpiration. Previous research has similarly found decreasing AC1 in the enhanced vegetation index in tundra regions in North America [36]. Additionally, signals of flickering in transpiration may reflect more frequent excursions into alternative regimes (e.g., snow vs. rain, frozen vs. thawed) brought on by increasing global temperatures [33].

We present a methodological approach to understand the extent to which EWS are useful in predicting abrupt shifts. We find limited, but non-negligible, added value of using EWS when predicting abrupt shifts, and demonstrate that including only CSD as a leading indicator of critical transitions may be misleading. Ecosystems themselves differ in their soil–water–vegetation coupling dynamics, water availability adaptation strategies, plant-stress regimes, and the temporal scales of dominant forcing variables. For these reasons, a single EWS is likely to be insufficient. Instead, we find a wider portfolio of context appropriate EWS may be warranted. The differences in the relative importance of some EWS compared to other indicators across aridity classes also suggest that the predictive power of EWS depends on climatic and ecosystem characteristics. This is critical for understanding where one might expect EWS to be informative. While we find EWS may not be broadly powerful predictors on their own, they could provide important information when combined with environmental context and a plausible understanding of where a signal may be ecologically informative. We also highlight that resilience assessments may benefit from accounting for these potential multiple pathways by adopting a multiple indicator approach.

By focusing on non-linear changes to green water variables, we provide a complementary perspective to previous research on related aspects of water resilience [5, 37]. Non-linear responses are expected when a state variable's response to a forcing is neither gradual nor proportional to the magnitude of the disturbance, consistent with threshold and feedback-related processes in the water cycle [38–42].

Our findings add an important empirical perspective on the global stability of key water cycle components, and we further identify several avenues for future research. Integrating analysis from direct measurements and ground networks (e.g., flux tower measurements, in-situ soil moisture) could help to better resolve spatial heterogeneity that coarse satellite products cannot capture. CSD theory presumes a slow approach to a single driver-induced bifurcation, whereas terrestrial systems are typically subject to interacting and evolving drivers [43, 44], for example, projected changes in the strength and spatial pattern of climate oscillations [45, 46]. We show that including information on drivers improves the ability of EWS to predict abrupt shifts. Improved understanding of the local, distal, and interacting temporal and spatial influence of these drivers, can further inform long-term ecosystem management strategies, and contribute to safeguarding water as a critical stabilising force in the Earth system.

4 Methods

4.1 Data

We derived weekly time series of three key green water variables (transpiration, E_t; soil moisture, SM; and precipitation, P) from remotely sensed datasets, aggregated to a spatial resolution of 0.25°, from 2000 to 2023. Transpiration data were retrieved from GLEAM v4.2 (Global Land Evaporation Amsterdam Model, 0.1°, 1980 – 2023) [47], which combines remote-sensing observations with model outputs, and uses Penman-Monteith's equation to calculate potential evaporation (E_{pot}). GLEAM uses satellite data to estimate E_t, and has been validated against in situ eddy-covariance data. Surface soil moisture data was retrieved from ESA CCI (European Space Agency Climate Change Initiative, 0.25°, 1978 - 2023) [48–50], which combines passive and active microwave sensors. ESA CCI SM has global coverage with the exception of tropical moist forests. The combined product has been corrected for structural breaks in the time series that arise from sensor merging. Precipitation data were retrieved from PERSIANN-CDR (Precipitation Estimation from Remotely Sensed Information using Artificial Neural Networks - Climate Data Record, 0.25°, 1983 - present, with a coverage of 60°S to 60°N) [51].

Single-sensor remote sensing time series are preferred in EWS assessments of resilience loss. For soil moisture, where long, single-sensor time series were not available, we used remotely sensed data that have been structurally corrected for changes to autocorrelation and variance in the merging procedure (ESA CCI SM) [50]. For precipitation, PERSIANN-CDR does not use cumulative distribution function matching for time series merging, or require posteriori distribution or bias correction [52], as this is handled directly by the neural network [53]. Sensor changes can result in changes in the signal-to-noise ratio and variance [54, 55], and the merging procedures that produce a continuous data record generally do not account for data artefacts in the higher statistical moments of the time series distribution [15, 56]. These may be erroneously interpreted as signals of resilience loss [24].

4.2 Resilience loss theory and detection

EWS describe a set of statistical methods for detecting resilience loss, which are based on the rationale that a systems' recovery rate to equilibrium after a disturbance changes as the system loses resilience [15, 57].

A change in the recovery rate of a system can be measured by changes in autocorrelation and variance [12]. Simultaneously increasing autocorrelation and variance indicate both an increased tendency for the system properties to be distributed further from its equilibrium, and a slower recovery back to its equilibrium: the basin of attraction becomes wider and shallower. This indicates that a system's recovery rate after disturbances or stochastic perturbations is slowing as the system state becomes increasingly correlated with past states, termed **Critical Slowing Down (CSD)**. CSD applies only when external conditions gradually move the system towards a potential regime shift [58], also known as bifurcation tipping [59]. However, as natural systems are largely embedded in stochastic environments, the observability of a gradual increase in autocorrelation and variance alone may be limited [13, 24].

Recent studies have shown that the influence of multiple drivers, changes to the driving variable structure, or noise regime can modulate CSD signals, warranting attention not only to simultaneous increases, but also to mixed signals and simultaneous decreases [22, 23]. Research has shown experimentally that multiple drivers acting on a system simultaneously can produce contradictory signals [22]; increasing autocorrelation and decreasing variance, or vice-versa. Further, the dynamics of an ecosystem experiencing perturbations, such as increasing dry spells, may appear increasingly autocorrelated without approaching a critical threshold should the perturbation regime itself become increasingly autocorrelated [58]. They also find that the variance of the state variable may decrease prior to a critical threshold, should the state variables sensitivity to a forcing variable change over time.

Critical Speeding Up (CSU) is an alternative phenomenon of resilience loss and emerges in highly stochastic systems, given by a narrowing of the basin of attraction [23]. As this basin becomes smaller, the likelihood of a system occupying the smaller basin likewise becomes smaller, thereby reducing resilience, and leaving it more vulnerable to noise-induced (i.e. stochastic) transitions [23, 59]. With a single slowly changing forcing variables, decreasing autocorrelation and variance may indicate greater local stability. However, in stochastic environments, it may signal an increased vulnerability to noise associated with a shrinking basin of attraction.

Flickering is detected by changing skewness, and kurtosis or variance, and has been proposed as an alternative method for highly stochastic systems [60, 61]. Fundamentally, changes to the skewness and kurtosis of a system indicate an increasing tendency for the system state to exist at the extremes of its distribution. Flickering measures brief excursions of the system to an alternative regime, where external conditions may push the system temporarily closer to a critical threshold [13, 62, 63].

The fractal dimension, closely related to the Hurst Exponent, is a scale-free measure of the self-similarity or long-term memory of a time series [64]. A decrease in the fractal dimension indicates decreasing long-term memory, or increasing self-similarity. While autocorrelation and variance may pick up an increase in noise over time as a signal of resilience loss, the fractal dimension is more robust to this type of non-stationarity in a time series [65].

In complex systems, multiple drivers affect the chosen state variable, each operating on different temporal scales. Each driver may affect system recovery time and stability in a way that is not captured by a single indicator. To account for this, we implement a multiple working hypothesis approach [66]. We include assessments of five statistical indicators typically included in EWS assessments: the autocorrelation and standard deviation (CSD; [12, 13, 58, 67], CSU; [23]), skewness and kurtosis (flickering; [60, 62, 68]), and the fractal dimension [64, 65, 69]. For autocorrelation and standard deviation, we also report regions showing mixed signals, where one increases and the other decreases, and vice versa.

Because EWS are based on fluctuations of state variables about their equilibrium [70], the time series are first de-trended and de-seasoned by applying a Seasonal-Trend decomposition using LOESS filter to remove natural periodicities, inter-annual (1-year) and inter-decadal modes of climate variability (5-years) [24]. Then, for all pixels, the first difference of the resulting residual time series is used to calculate the EWS, to remove as much residual periodicity from the time series as possible. To measure the temporal evolution of autocorrelation, variance, skewness, kurtosis, and the fractal dimension, we calculate each of the EWS indicators within a 5-year rolling window, for each pixel globally (Figure 6).

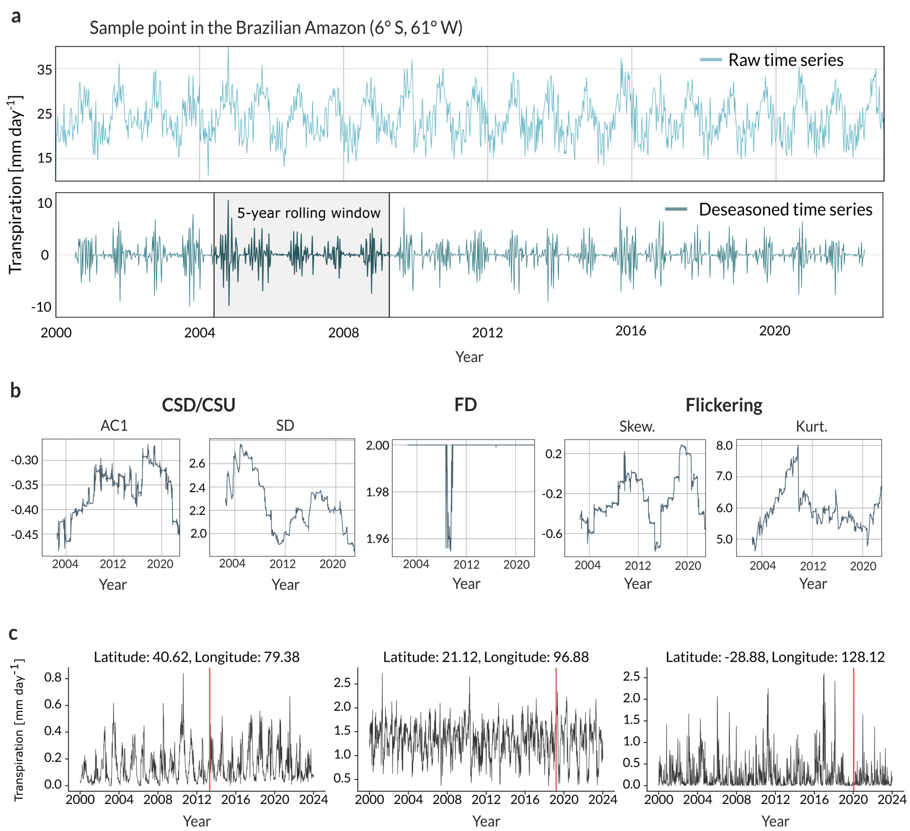

Fig. 6 Analysis example for transpiration. Panels (a - c) exemplify the analysis method used. (a) Raw and de-seasoned time series for transpiration for a pixel in the Brazilian Amazon, with 5-year rolling window over which the EWS are calculated, overlaid. (b) Five indicators are computed for the pixel on the de-seasoned time series, over the rolling window. Autocorrelation (AC1) and standard deviation (SD) are associated with Critical Slowing Down (CSD) and Critical Speeding Up (CSU); skewness (Skew.), and kurtosis (Kurt.) are associated with flickering; the fractal dimension (FD) is interpreted alone. (c) Exemplary pixels where an abrupt shift in transpiration was detected; the red vertical line marks the estimated year of shift.

We calculate three different statistics of the change in the five EWS indicators to obtain a comprehensive understanding: the Kendall's τ is used to determine the significance of a monotonic trend [71]; the Thiel-Sen slope is used to quantify the magnitude of the trend [72, 73]; and the change in mean at half the time series is used to quantify the overall shift between the first and second half of the time-series, where significance was determined using a two-sided t-test [19]. For a comparison of the agreement across tests, see Supplementary Fig. 6. As an additional measure, we calculate the time-ordered difference between maximum and minimum of each EWS, delta, to yield the maximum change over the time-series length [16]. For the computation of statistics, we exclude pixels that contain more than 3% built environment using land cover masks from the Copernicus Global Land Service [74]. Pixels that contain more than 25% crop cover and are predominantly non-irrigated (based on area equipped for irrigation [75]) are treated separately as an artificial rain-fed cropland biome.

4.3 Estimating abrupt shifts

We identify abrupt shifts for the three green water variables using the raw variable time series. The set of identified abrupt shifts serves as empirical ground-truth of where green water dynamics have abruptly and significantly changed. Abrupt shifts are detected using the R package 'strucchange' [76, 77], which is a breakpoint detection method which applies a structural change test to fitted autoregressive model (AR1) of the time series. For each pixel, we fit an autoregressive model, where the variable at time x_t is regressed on its lag at x_{t-1}, and computed the supF statistic [26]. A breakpoint is identified at the time where the regression intercept (mean) and/or the autoregressive processes governing the time series changed significantly ($p < 0.05$ from the supF test). We interpreted these breakpoints as the point in time when short-term dynamics governing the time series change, thus representing abrupt shifts in variable dynamics. We then compute the mean before (m_1) and after (m_2) the breakpoint, and report both absolute ($m_2 - m_1$) and proportional (m_2/m_1) changes. We report the results from the structural change approach, because it is statistically more conservative and appears less prone to spurious detections than tests based solely on mean or variance shift, given that it jointly tests for shifts in mean and short-term memory processes.

4.4 Evaluating EWS efficacy

We assume that, should a structural change in green water properties at a pixel have occurred, such a change would manifest as a detected abrupt shift in the time series, with a preceding EWS. To better understand if EWS can predict the detected abrupt shift binary target, we developed a machine learning framework to train three boosted regression classification models, one for each green water variable. Boosted regression models are tree-based machine learning models that are able to capture interactions and non-linear patterns between predictor variables [78]. The target variables for each model were whether or not an abrupt shift was detected (True/False; positive or negative class, respectively), and the features, or explanatory variables used to predict the target variable, are the Kendall's τ of the EWS (Section 4.2) and several environmental variables to represent the hydrological, ecological, and climatic features of each pixel. The environmental variables included in the models, the green water variable for which they were applied, and dataset sources listed in Supplementary Table 9. The environmental variables were resampled to a 0.25° spatial resolution to match the resolution of the target variables, and resampled to monthly time-scales where needed. These variables were added as static features: including only the mean, standard deviation, and linear trend over time of the variable.

To prevent systematic distributional differences of the EWS Kendall's τ between the positive and negative classes being picked up by the models, the EWS feature variables were created separately and then combined with the environmental variables. For the positive class, we re-calculated the EWS and Kendall's τ on the time series preceding the abrupt shift. We did this for all pixels where the breakpoints detected using the supF-statistic were significant, and occurred at least 12 years after the start of the time series, to ensure a sufficient number of time steps for the EWS calculation and to account for the rolling window length. For the negative class, to construct the EWS variables in a symmetrical way, we generate a distribution of breakpoint time stamps from the positive class, and randomly sample time steps from this distribution, assigning them to pixels in the negative class. We then re-calculate Kendall's τ of the EWS before this randomly assigned breakpoint, or pseudo-breakpoint. The explanatory variables in the models therefore include the Kendall's τ of each of the five studied EWS (Section 4.2) either before the breakpoint for the positive class, or before a pseudo-breakpoint for the negative class, and the environmental variables over the whole time series. Machine learning models are not based on a mechanistic representation of processes, so they cannot directly provide causal information on how features influence the system response. Rather, the explanatory variables describe environmental characteristics and EWS signals, at each pixel that may contribute to the detection of an abrupt shift.

Because positive cases (detected abrupt shifts) are relatively rare at the global scale, we apply a class weighting to address class imbalance. We retain the full dataset, but apply a weight proportional to the negative-to-positive class ratio during model training and performance evaluation. Given that breakpoints were clustered in space, we implement a spatial, blocked cross-validation to account for potential spatial autocorrelation [79]. Specifically, the global domain was partitioned into $10^{\circ} \times 10^{\circ}$ latitude–longitude blocks where each block is randomly assigned to one of five cross-validation folds, or subsets, so calibration and validation occurs on spatially separated regions. This results in an 80% and 20% training and testing split. The 10° size was chosen as a practical compromise between reducing spatial leakage and retaining sufficiently heterogenous training data per subset. Model performance is therefore assessed by training the model on four subsets, and evaluating on the held-out fifth, for all five subsets [79]. Further details on the model training can be found in Supplementary Table 10 and Supplementary Fig. 11. Given that the abrupt shifts detected are relatively rare events, we report the precision-recall area-under-the-curve (PR AUC) and average precision (AP) to quantify model performance as threshold-agnostic performance metrics that remains informative under significant imbalance between positive and negative classes [80]. We then calculate Partial Dependence Plots (PDPs; [78]) and SHAP values [81] to provide explanations of feature effects and contributions to detecting abrupt shifts. To isolate the predictive value of EWS as predictors relative to the environmental variables as predictors, we also train two additional models per green water variable that contain either only the EWS as predictors, only the environmental variables as predictors, and compare these to the model performance with the full predictor set.

4.5 Sensitivity analysis

We conduct a sensitivity analysis to verify that our inferences are robust across calculation set-ups. We calculate the EWS and Kendall's τ for a 50 by 50 pixel tile, or 12.5° by 12.5°, in South America. We vary: (1) the sampling frequency (weekly, monthly), (2) window size over which EWS are calculated (2.5-years, 5-years, 10-years), and (3) de-trending choices (STL robust; first-differencing). For each configuration we map the Kendall's τ sign to three class labels (-1, 0, $+1$; negative τ, no change, positive τ), where $|\tau| \leq 0.05$ and $p > 0.05$ are treated as 0. For each configuration, we calculate the pair-wise Cohen's κ [82] and report the average agreement across all configurations, adjusted for chance (Light's κ [83]). This allows us to capture whether two configurations give the same sign, or show now change, at the same pixel, measuring the pixel-wise agreement between chosen parameter configurations. Cohen's κ denotes how much two maps of Kendall's τ agree on the sign of change, beyond what would be expected by chance, where $\kappa = 1$ is perfect agreement, $\kappa = 0$ is no better than chance, and $\kappa < 0$ indicates disagreement. To measure the effect of one configuration change, we create pairs of configurations that are identical on the other three factors and differ only in the configuration we want to measure the effect of. We then compute Cohen's

κ for each such pairs maps, averaging κ across the pairs. Light's κ is the pairwise average κ across all configurations, calculated per indicator (Supplementary Table 1).

Transpiration. Across configurations, Light's κ is highest for AC1 ($\kappa = 0.16$), followed by FD, kurtosis, SD, and skewness (mean κ across indicators = 0.116). Sampling frequency (weekly vs. monthly) is the largest source of sensitivity (mean κ across indicators = -0.01), indicating systematic pixel-wise disagreement between monthly and weekly data. Changing only the window length gives a mean κ of 0.4 across indicators, indicating relative stability. First differencing has a lower mean κ across indicators (0.24), indicating moderate stability (Supplementary Table 1).

Soil moisture. Overall agreement is higher for soil moisture across configurations; SD is most stable (Light's $\kappa = 0.56$), followed by kurtosis, FD, AC1, and skewness (mean κ across indicators = 0.23). First differencing is the largest source of sensitivity, resulting in the lowest mean κ for AC1, FD, kurtosis, and skewness (0.16, 0.06, 0.11, -0.03, respectively); SD remains high (0.71). Changing either only the window length or sampling frequency results in a higher agreement (mean κ across indicators = 0.487 and 0.318, respectively) (Supplementary Table 1).

Precipitation. Light's κ is highest for SD ($\kappa = 0.30$), followed by AC1, FD, kurtosis and skewness (κ across indicators = 0.19). Sampling frequency is again the largest source of sensitivity, having the greatest effect on pixel-wise sign agreement. Between weekly and monthly temporal aggregation, mean κ is 0.17 for SD and ≈ 0.03 for the remaining variables. With a fixed sampling frequency, mean κ is higher for the other configurations. Changing window lengths gives mean $\kappa = 0.52$ across EWS. The first differencing configuration gives mean $\kappa = 0.36$, for SD, AC1, FD, and kurtosis. Skewness is sensitive to first differencing (mean $\kappa = -0.03$), signalling disagreement (Supplementary Table 1).

We choose weekly sampling frequency to preserve seasonal variability and maximise observations per sampling window, although we note that results are sensitive to the chosen sampling frequency. Given that results are relatively stable across window lengths, we choose a 5-year window as a compromise between adequate sample size and temporal smoothening.

Further, to assess the sensitivity of the results to trend estimation approach, we compare three approaches for each indicator (AC1, SD, FD, Skew, Kurt) and check for agreement in sign of change: KT (Kendall's τ, $p < 0.05$), TS (Theil–Sen slope, $p < 0.05$), Δ (time-ordered difference between maximum and minimum), and MC (mean-change between time series halves, Welch's t-test $p < 0.05$) (Supplementary Fig. 6). Each pixel is assigned a class of -1, 0, or +1 (corresponding to a decrease, no change, or an increase). The pairwise comparisons use all grid cells (n = 1 036 800). We report the linear-weighted Cohen's κ [82]. Weights are 1 where both show agreement in sign, 0.5 where signs are adjacent (i.e. increasing and no change, or decreasing and no change), and 0 for opposite signs. KT and TS slope agree for AC1, SD, Skew., Kurt. ($\kappa_w \geq 0.997$) on trend direction across variables (Supplementary Fig. 6). MC vs KT/TS shows high agreement for AC1, SD, Skew., Kurt. ($\kappa_w \approx$ 0.85–0.89). The time-ordered difference (δ) has very low agreement with other tests ($\kappa_w \approx$ 0.02–0.07). Relatively fewer pixels that showed a significant change in FD were detected using the Theil-Sen test, which therefore shows weak agreement with MC and KT across green water variables ($0.05 \leq \kappa_w \geq 0.25$). While AC1, SD, Skew., and Kurt. show strong agreement across methods, we find FD is sensitive to the choice of trend estimator.

Supplementary information. This article has accompanying supplementary information.

Acknowledgements. We thank M. Kummu and A. Hattle for their helpful comments on the manuscript.

Declarations

5 Funding

This manuscript is a product of the Formas project SAFER with grant number 2022-02089. Additionally, L.W-E is further supported by funding from Formas - a Swedish Research Council for Sustainable Development (ESI 2023-00310, ReForMit 2023-00321, and SOS-Cryo 2024-01655), the IKEA foundation, and Horizon Europe (WorldTrans 101081661); J.C.R. and N.K. are supported by VR grant 2022-04122.

6 Competing interests

The authors declare no competing interests.

7 Ethics approval and consent to participate

Not applicable

8 Consent for publication

Not applicable

9 Data availability

All data was retrieved from publicly available, open datasets: GLEAM version 4.2 daily transpiration (https://www.gleam.eu/); PERSIANN-CDR daily precipitation (https://chrsdata.eng.uci.edu/); ESA-CCI SM combined sensor daily soil moisture (https://climate.esa.int/en/projects/soil-moisture/); Copernicus Land Monitoring Service crop and urban land cover fractions (https://land.copernicus.eu/en/global). For the machine learning analysis 2-meter temperature, 2-meter dew-point temperature, relative humidity, total precipitation, volumetric soil moisture, transpiration, boundary layer height, convective available potential energy, and forecast albedo, were retrieved from the Earth Retrospective Analysis 5 (ERA5) monthly averaged data on single levels (https://cds.climate.copernicus.eu/datasets/reanalysis-era5-single-levels-monthly-means); hourly potential evapotranspiration was retrieved from (ref.[84], https://doi.org/10.5523/bris.qb8ujazzda0s2aykkv0oq0ctp); groundwater table depth was retrieved from (ref.[85], http://thredds-gfnl.usc.es/thredds/catalog/GLOBALWTDFTP/catalog.html); crop cover data was retrieved from Global Food-and-Water Security-support Analysis Data (GFSAD) (https://www.usgs.gov/centers/western-geographic-science-center/science/global-food-and-water-security-support-analysis); MODIS/Terra Gross Primary Productivity 8-Day L4 Global 500m SIN Grid V061 was retrieved from (https://www.earthdata.nasa.gov/data/catalog/lpcloud-mod17a2h-061); tree cover and non-tree vegetation cover were retrieved from MODIS-/Terra Vegetation Continuous Fields Yearly L3 Global 250m SIN Grid V006 (https://www.earthdata.nasa.gov/data/catalog/lpcloud-mod44b-006); ENSO index was retrieved from NASA-SSH ENSO Sea Surface Height Indicator (https://podaac.jpl.nasa.gov/dataset/NASA_SSH_ENSO_INDICATOR).

10 Materials availability

Not applicable

11 Code availability

All code used in the analysis of the raw data to produce the primary results is available on GitHub (https://github.com/romlotch/25_09_water_resilience_ews).

12 Author contribution

R.L.: Conceptualization, Methodology, Software, Validation, Formal analysis, Investigation, Writing – original draft, Writing – review & editing, Visualization. **N.K.**: Software, Writing – review & editing. **L.W-E.**: Conceptualisation, Investigation, Writing – review & editing, Supervision, Project administration, Funding acquisition. **J.C.R.**: Conceptualisation, Investigation, Writing – review & editing, Supervision, Project administration, Funding acquisition.

Appendix A Extended Data

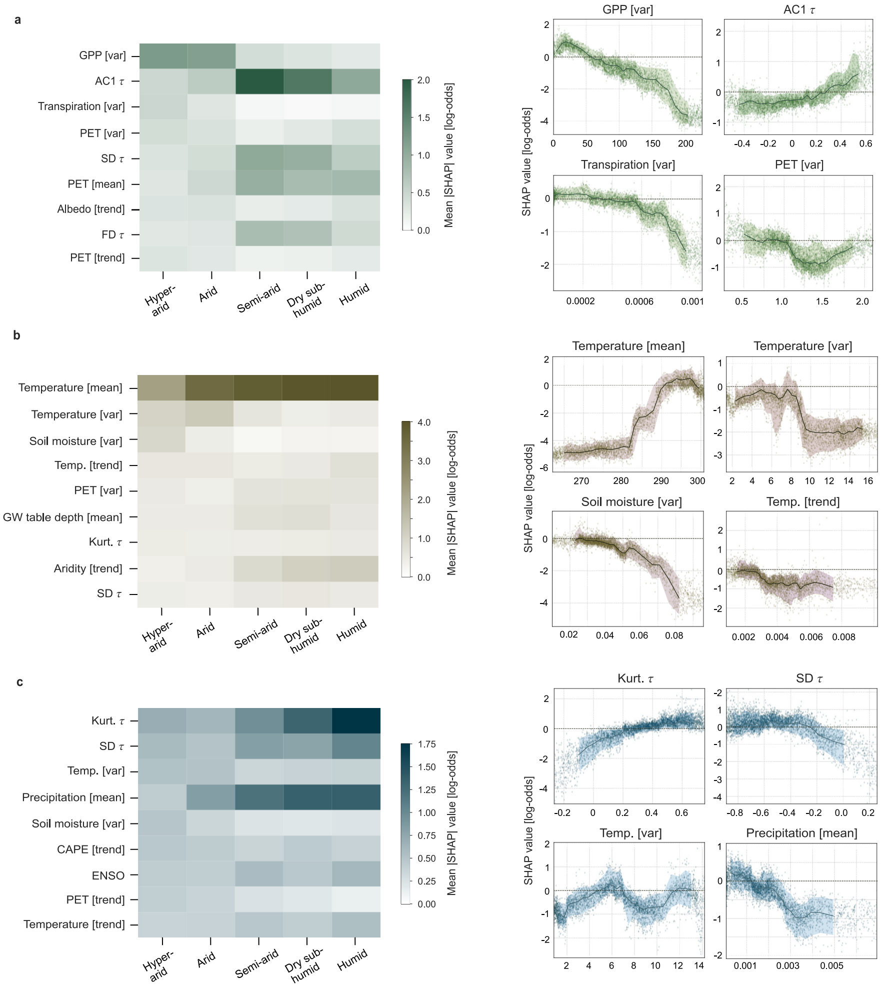

Fig. A1 Model interpretability with SHAP values across aridity classes for transpiration (a), soil moisture (b), and precipitation (c). Heatmaps show SHAP values for the top 10 predictors with the highest contribution to the model predictions, with rows organised by mean absolute SHAP importance across aridity classes, and SHAP dependence plots of the four most important predictors, show feature value (x-axis) against SHAP log-odds (y-axis), representing its contribution to model predictions. Positive values increase the predicted probability of an abrupt shift, negative values decrease it.

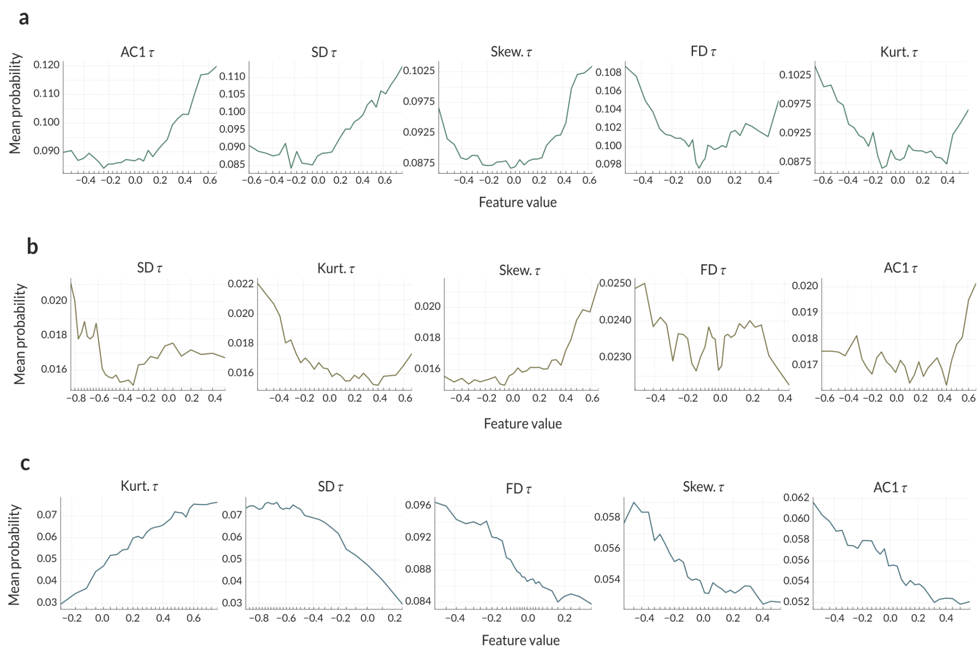

Fig. A2 Partial dependence plots of the individual EWS indicators for transpiration (a), soil moisture (b), and precipitation (c). Plots are ordered according to global variable importances for each green water variable, where the leftmost plot is the EWS with the highest variable importance, and rightmost is the least. Higher values indicate the EWS value that is associated with a higher probability of detecting an abrupt shift.

References

[1] Gleeson, T. *et al.* Illuminating water cycle modifications and Earth system resilience in the Anthropocene. *Water Resources Research* **56** (2020). Publisher: American Geophysical Union (AGU).

[2] Falkenmark, M. & Wang-Erlandsson, L. A water-function-based framework for understanding and governing water resilience in the Anthropocene. *One Earth* **4**, 213–225 (2021). Publisher: Elsevier BV.

[3] Wang-Erlandsson, L. *et al.* A planetary boundary for green water. *Nature Reviews Earth &amp\mathsemicolon Environment* **3**, 380–392 (2022). Publisher: Springer

Science and Business Media LLC.

[4] Porkka, M. *et al.* Global water cycle shifts far beyond pre-industrial conditions – planetary boundary for freshwater change transgressed (2023). Publisher: California Digital Library (CDL).

[5] Nie, W. *et al.* Nonstationarity in the global terrestrial water cycle and its interlinkages in the Anthropocene. *Proceedings of the National Academy of Sciences* **121**, e2403707121 (2024). URL https://www.pnas.org/doi/abs/10.1073/pnas.2403707121. Company: National Academy of Sciences Distributor: National Academy of Sciences Institution: National Academy of Sciences Label: National Academy of Sciences Publisher: Proceedings of the National Academy of Sciences.

[6] Falkenmark, M., Wang-Erlandsson, L. & Rockström, J. Understanding of water resilience in the Anthropocene. *Journal of Hydrology X* **2**, 100009 (2019). Publisher: Elsevier BV.

[7] Zemp, D. C., Schleussner, C.-F., Barbosa, H. M. J. & Rammig, A. Deforestation effects on Amazon forest resilience. *Geophysical Research Letters* **44**, 6182–6190 (2017). URL https://onlinelibrary.wiley.com/doi/abs/10.1002/2017GL072955. _eprint: https://onlinelibrary.wiley.com/doi/pdf/10.1002/2017GL072955.

[8] Staal, A. *et al.* Feedback between drought and deforestation in the Amazon. *Environmental Research Letters* **15**, 044024 (2020). URL https://dx.doi.org/10.1088/1748-9326/ab738e. Publisher: IOP Publishing.

[9] Yang, L., Sun, G., Zhi, L. & Zhao, J. Negative soil moisture-precipitation feedback in dry and wet regions. *Scientific Reports* **8** (2018). Publisher: Springer Science and Business Media LLC.

[10] Berdugo, M. *et al.* Global ecosystem thresholds driven by aridity. *Science* **367**, 787–790 (2020). Publisher: American Association for the Advancement of Science (AAAS).

[11] Holling, C. S. Resilience and Stability of Ecological Systems. *Annual Review of Ecology and Systematics* **4**, 1–23 (1973). Publisher: Annual Reviews.

[12] Scheffer, M. *et al.* Early-warning signals for critical transitions. *Nature* **461**, 53–59 (2009). Publisher: Springer Science and Business Media LLC.

[13] Dakos, V., Carpenter, S. R., van Nes, E. H. & Scheffer, M. Resilience indicators: prospects and limitations for early warnings of regime shifts. *Philosophical Transactions of the Royal Society B: Biological Sciences* **370**, 20130263 (2015). URL https://royalsocietypublishing.org/doi/full/10.1098/rstb.2013.0263. Publisher: Royal Society.

[14] Dakos, V. & Kéfi, S. Ecological resilience: what to measure and how. *Environmental Research Letters* **17**, 043003 (2022). Publisher: IOP Publishing.

[15] Dakos, V. *et al.* Tipping point detection and early warnings in climate, ecological, and human systems. *Earth System Dynamics* **15**, 1117–1135 (2024). Publisher: Copernicus GmbH.

[16] Rocha, J. C. Ecosystems are showing symptoms of resilience loss. *Environmental Research Letters* **17**, 065013 (2022). Publisher: IOP Publishing.

[17] Smith, T., Traxl, D. & Boers, N. Empirical evidence for recent global shifts in vegetation resilience. *Nature Climate Change* **12**, 477–484 (2022). URL https://www.nature.com/articles/s41558-022-01352-2. Publisher: Nature Publishing Group.

[18] Feng, Y. *et al.* Reduced resilience of terrestrial ecosystems locally is not reflected on a global scale. *Communications Earth & Environment* **2**, 1–11 (2021). URL https://www.nature.com/articles/s43247-021-00163-1. Publisher: Nature Publishing Group.

[19] Forzieri, G., Dakos, V., McDowell, N. G., Ramdane, A. & Cescatti, A. Emerging signals of declining forest resilience under climate change. *Nature* **608**, 534–539 (2022). URL https://www.nature.com/articles/s41586-022-04959-9. Publisher: Nature Publishing Group.

[20] Verbesselt, J. *et al.* Remotely sensed resilience of tropical forests. *Nature Climate Change* **6**, 1028–1031 (2016). URL https://www.nature.com/articles/nclimate3108. Publisher: Nature Publishing Group.

[21] Knecht, N., Lotcheris, R. A., Fetzer, I. & Rocha, J. Complex Realities, Simple Signals? Global Evaluation of Early Warning Signals for Forest Mortality Events. *EGUsphere* 1–42 (2025). URL https://egusphere.copernicus.org/preprints/2025/egusphere-2025-4902/. Publisher: Copernicus GmbH.

[22] Dai, L., Korolev, K. S. & Gore, J. Relation between stability and resilience determines the performance of early warning signals under different environmental drivers. *Proceedings of the National Academy of Sciences* **112**, 10056–10061 (2015). Publisher: Proceedings of the National Academy of Sciences.

[23] Titus, M. & Watson, J. Critical speeding up as an early warning signal of stochastic regime shifts. *Theoretical Ecology* **13**, 449–457 (2020). URL https://doi.org/10.1007/s12080-020-00451-0.

[24] Smith, T. & Boers, N. Reliability of vegetation resilience estimates depends on biomass density. *Nature Ecology & Evolution* **7**, 1799–1808 (2023).

Publisher: Springer Science and Business Media LLC.

[25] Boettiger, C. & Hastings, A. No early warning signals for stochastic transitions: insights from large deviation theory. *Proceedings of the Royal Society B: Biological Sciences* **280**, 20131372 (2013). Publisher: The Royal Society.

[26] Andersen, T., Carstensen, J., Hernández-García, E. & Duarte, C. M. Ecological thresholds and regime shifts: approaches to identification. *Trends in Ecology & Evolution* **24**, 49–57 (2009). URL https://www.sciencedirect.com/science/article/pii/S0169534708003054.

[27] Smith, T. & Boers, N. Global vegetation resilience linked to water availability and variability. *Nature Communications* **14**, 498 (2023). URL https://www.nature.com/articles/s41467-023-36207-7. Publisher: Nature Publishing Group.

[28] Seddon, A. W. R., Macias-Fauria, M., Long, P. R., Benz, D. & Willis, K. J. Sensitivity of global terrestrial ecosystems to climate variability. *Nature* **531**, 229–232 (2016). URL https://www.nature.com/articles/nature16986. Publisher: Nature Publishing Group.

[29] Huang, J., Yu, H., Guan, X., Wang, G. & Guo, R. Accelerated dryland expansion under climate change. *Nature Climate Change* **6**, 166–171 (2016). URL https://www.nature.com/articles/nclimate2837. Publisher: Nature Publishing Group.

[30] Li, W. *et al.* Widespread increasing vegetation sensitivity to soil moisture. *Nature Communications* **13**, 3959 (2022). URL https://www.nature.com/articles/s41467-022-31667-9. Publisher: Nature Publishing Group.

[31] Boulton, C. A., Lenton, T. M. & Boers, N. Pronounced loss of Amazon rainforest resilience since the early 2000s. *Nature Climate Change* **12**, 271–278 (2022). URL https://www.nature.com/articles/s41558-022-01287-8. Publisher: Nature

Publishing Group.

[32] Walvoord, M. A. & Kurylyk, B. L. Hydrologic Impacts of Thawing Permafrost—A Review. *Vadose Zone Journal* **15**, vzj2016.01.0010 (2016). URL https://doi.org/10.2136/vzj2016.01.0010.

[33] Calvin, K. *et al.* IPCC, 2023: Climate Change 2023: Synthesis Report. Contribution of Working Groups I, II and III to the Sixth Assessment Report of the Intergovernmental Panel on Climate Change [Core Writing Team, H. Lee and J. Romero (eds.)]. IPCC, Geneva, Switzerland. Tech. Rep., Intergovernmental Panel on Climate Change (IPCC) (2023). URL https://www.ipcc.ch/report/ar6/syr/. Edition: First.

[34] Myers-Smith, I. H. *et al.* Shrub expansion in tundra ecosystems: dynamics, impacts and research priorities. *Environmental Research Letters* **6**, 045509 (2011). URL https://dx.doi.org/10.1088/1748-9326/6/4/045509. Publisher: IOP Publishing.

[35] Macias-Fauria, M., Forbes, B. C., Zetterberg, P. & Kumpula, T. Eurasian Arctic greening reveals teleconnections and the potential for structurally novel ecosystems. *Nature Climate Change* **2**, 613–618 (2012). URL https://www.nature.com/articles/nclimate1558. Publisher: Nature Publishing Group.

[36] Zhang, Y. *et al.* Warming and disturbances affect Arctic-boreal vegetation resilience across northwestern North America. *Nature Ecology & Evolution* **8**, 2265–2276 (2024). URL https://www.nature.com/articles/s41559-024-02551-0. Publisher: Nature Publishing Group.

[37] Porkka, M. *et al.* Notable shifts beyond pre-industrial streamflow and soil moisture conditions transgress the planetary boundary for freshwater change.

Nature Water **2**, 262–273 (2024). URL https://www.nature.com/articles/s44221-024-00208-7. Publisher: Nature Publishing Group.

[38] Kéfi, S., Rietkerk, M., van Baalen, M. & Loreau, M. Local facilitation, bistability and transitions in arid ecosystems. *Theoretical Population Biology* **71**, 367–379 (2007). URL https://www.sciencedirect.com/science/article/pii/S0040580906001250.

[39] Gentine, P. *et al.* Coupling between the terrestrial carbon and water cycles—a review. *Environmental Research Letters* **14**, 083003 (2019). URL https://dx.doi.org/10.1088/1748-9326/ab22d6. Publisher: IOP Publishing.

[40] Bassiouni, M., Good, S. P., Still, C. J. & Higgins, C. W. Plant Water Uptake Thresholds Inferred From Satellite Soil Moisture. *Geophysical Research Letters* **47**, e2020GL087077 (2020). URL https://onlinelibrary.wiley.com/doi/abs/10.1029/2020GL087077. _eprint: https://agupubs.onlinelibrary.wiley.com/doi/pdf/10.1029/2020GL087077.

[41] Seneviratne, S. I. *et al.* Investigating soil moisture–climate interactions in a changing climate: A review. *Earth-Science Reviews* **99**, 125–161 (2010). URL https://www.sciencedirect.com/science/article/pii/S0012825210000139.

[42] Zhang, Q. *et al.* Water limitation regulates positive feedback of increased ecosystem respiration. *Nature Ecology & Evolution* **8**, 1870–1876 (2024). URL https://www.nature.com/articles/s41559-024-02501-w. Publisher: Nature Publishing Group.

[43] Rocha, J. C., Peterson, G., Bodin, & Levin, S. Cascading regime shifts within and across scales. *Science* **362**, 1379–1383 (2018). URL https://www.science.org/doi/10.1126/science.aat7850. Publisher: American Association for the Advancement of Science.

[44] Zhou, G. *et al.* Resistance of ecosystem services to global change weakened by increasing number of environmental stressors. *Nature Geoscience* **17**, 882–888 (2024). URL https://www.nature.com/articles/s41561-024-01518-x. Publisher: Nature Publishing Group.

[45] Kornhuber, K. *et al.* Amplified Rossby waves enhance risk of concurrent heatwaves in major breadbasket regions. *Nature Climate Change* **10**, 48–53 (2019). Publisher: Springer Science and Business Media LLC.

[46] Hu, K., Huang, G., Huang, P., Kosaka, Y. & Xie, S.-P. Intensification of El Niño-induced atmospheric anomalies under greenhouse warming. *Nature Geoscience* **14**, 377–382 (2021). URL https://www.nature.com/articles/s41561-021-00730-3. Publisher: Nature Publishing Group.

[47] Miralles, D. G. *et al.* GLEAM4: global land evaporation and soil moisture dataset at 0.1° resolution from 1980 to near present. *Scientific Data* **12**, 416 (2025). URL https://www.nature.com/articles/s41597-025-04610-y. Publisher: Nature Publishing Group.

[48] Dorigo, W. *et al.* ESA CCI Soil Moisture for improved Earth system understanding: State-of-the art and future directions. *Remote Sensing of Environment* **203**, 185–215 (2017). URL https://www.sciencedirect.com/science/article/pii/S0034425717303061.

[49] Gruber, A., Scanlon, T., van der Schalie, R., Wagner, W. & Dorigo, W. Evolution of the ESA CCI Soil Moisture climate data records and their underlying merging methodology. *Earth System Science Data* **11**, 717–739 (2019). URL https://essd.copernicus.org/articles/11/717/2019/. Publisher: Copernicus GmbH.

[50] Preimesberger, W., Scanlon, T., Su, C.-H., Gruber, A. & Dorigo, W. Homogenization of Structural Breaks in the Global ESA CCI Soil Moisture Multisatellite

Climate Data Record. *IEEE Transactions on Geoscience and Remote Sensing* **59**, 2845–2862 (2021). URL https://ieeexplore.ieee.org/document/9165186.

[51] Ashouri, H. *et al.* PERSIANN-CDR: Daily Precipitation Climate Data Record from Multisatellite Observations for Hydrological and Climate Studies. *Bulletin of the American Meteorological Society* **96**, 69–83 (2015). URL https://journals.ametsoc.org/view/journals/bams/96/1/bams-d-13-00068.1.xml. Publisher: American Meteorological Society Section: Bulletin of the American Meteorological Society.

[52] Moesinger, L. *et al.* The global long-term microwave Vegetation Optical Depth Climate Archive (VODCA). *Earth System Science Data* **12**, 177–196 (2020). URL https://essd.copernicus.org/articles/12/177/2020/. Publisher: Copernicus GmbH.

[53] Skulovich, O. & Gentine, P. A Long-term Consistent Artificial Intelligence and Remote Sensing-based Soil Moisture Dataset. *Scientific Data* **10**, 154 (2023). URL https://www.nature.com/articles/s41597-023-02053-x. Publisher: Nature Publishing Group.

[54] Boulton, C. A., Lenton, T. M. & Boers, N. Reply to: Little evidence that Amazonian rainforests are approaching a tipping point. *Nature Climate Change* **13**, 1321–1323 (2023). Publisher: Springer Science and Business Media LLC.

[55] Tao, S. *et al.* A global long-term, high-resolution satellite radar backscatter data record (1992–2022\mathplus): merging C-band ERS/ASCAT and Ku-band QSCAT. *Earth System Science Data* **15**, 1577–1596 (2023). Publisher: Copernicus GmbH.

[56] Bathiany, S. *et al.* Ecosystem Resilience Monitoring and Early Warning Using Earth Observation Data: Challenges and Outlook. *Surveys in Geophysics* (2024). Publisher: Springer Science and Business Media LLC.

[57] Lindegren, M. *et al.* Early Detection of Ecosystem Regime Shifts: A Multiple Method Evaluation for Management Application. *PLoS ONE* **7**, e38410 (2012). Publisher: Public Library of Science (PLoS).

[58] Dakos, V., van Nes, E. H., D'Odorico, P. & Scheffer, M. Robustness of variance and autocorrelation as indicators of critical slowing down. *Ecology* **93**, 264–271 (2012). URL https://onlinelibrary.wiley.com/doi/abs/10.1890/11-0889.1. _eprint: https://onlinelibrary.wiley.com/doi/pdf/10.1890/11-0889.1.

[59] Ashwin, P., Wieczorek, S., Vitolo, R. & Cox, P. Tipping points in open systems: bifurcation, noise-induced and rate-dependent examples in the climate system. *Philosophical Transactions of the Royal Society A: Mathematical, Physical and Engineering Sciences* **370**, 1166–1184 (2012). Publisher: The Royal Society.

[60] Guttal, V. & Jayaprakash, C. Changing skewness: an early warning signal of regime shifts in ecosystems. *Ecology Letters* **11**, 450–460 (2008). URL https://onlinelibrary.wiley.com/doi/abs/10.1111/j.1461-0248.2008.01160.x. _eprint: https://onlinelibrary.wiley.com/doi/pdf/10.1111/j.1461-0248.2008.01160.x.

[61] Wang, R. *et al.* Flickering gives early warning signals of a critical transition to a eutrophic lake state. *Nature* **492**, 419–422 (2012). URL https://www.nature.com/articles/nature11655. Publisher: Nature Publishing Group.

[62] Dakos, V., van Nes, E. H. & Scheffer, M. Flickering as an early warning signal. *Theoretical Ecology* **6**, 309–317 (2013). URL https://doi.org/10.1007/s12080-013-0186-4.

[63] Chevalier, M. & Grenouillet, G. Global assessment of early warning signs that temperature could undergo regime shifts. *Scientific Reports* **8**, 10058 (2018). URL https://www.nature.com/articles/s41598-018-28386-x. Publisher: Nature Publishing Group.

[64] Gneiting, T., Ševčíková, H. & Percival, D. B. Estimators of Fractal Dimension: Assessing the Roughness of Time Series and Spatial Data. *Statistical Science* **27** (2012). Publisher: Institute of Mathematical Statistics.

[65] Bian, J., Ma, Z., Wang, C., Huang, T. & Zeng, C. Early warning for spatial ecological system: Fractal dimension and deep learning. *Physica A: Statistical Mechanics and its Applications* **633**, 129401 (2024). Publisher: Elsevier BV.

[66] Chamberlin, T. C. Studies for Students: The Method of Multiple Working Hypotheses. *The Journal of Geology* **5**, 837–848 (1897). Publisher: University of Chicago Press.

[67] Scheffer, M., Hirota, M., Holmgren, M., Van Nes, E. H. & Chapin, F. S. Thresholds for boreal biome transitions. *Proceedings of the National Academy of Sciences* **109**, 21384–21389 (2012). Publisher: Proceedings of the National Academy of Sciences.

[68] Ditlevsen, P. D. & Johnsen, S. J. Tipping points: Early warning and wishful thinking. *Geophysical Research Letters* **37** (2010). Publisher: American Geophysical Union (AGU).

[69] West, G. Scale: The Universal Laws of Growth, Innovation, Sustainability, and the Pace of Life in Organisms, Cities, Economies, and Companies: The Universal Laws of Life, Growth, and Death in Organisms, Cities, and Companies (2017). ISBN: 9781101621509 Num Pages: 10 Place: East Rutherford.

[70] Dakos, V. *et al.* Slowing down as an early warning signal for abrupt climate change. *Proceedings of the National Academy of Sciences* **105**, 14308–14312 (2008). URL https://www.pnas.org/doi/abs/10.1073/pnas.0802430105. Publisher: Proceedings of the National Academy of Sciences.

[71] Kendall, M. G. *Rank Correlation Methods* (C. Griffin, 1948).

[72] Sen, P. K. Estimates of the Regression Coefficient Based on Kendall's Tau. *Journal of the American Statistical Association* **63**, 1379–1389 (1968). URL https://www.jstor.org/stable/2285891. Publisher: [American Statistical Association, Taylor & Francis, Ltd.].

[73] Conover, W. J. *Practical nonparametric statistics* (New York : Wiley, 1980). URL http://archive.org/details/practicalnonpara0000cono.

[74] Buchhorn, M. *et al.* Copernicus Global Land Cover Layers—Collection 2. *Remote Sensing* **12**, 1044 (2020). URL https://www.mdpi.com/2072-4292/12/6/1044. Publisher: Multidisciplinary Digital Publishing Institute.

[75] Siebert, S., Doll, P. & Hoogeveen, J. Development and validation of the global map of irrigation areas. *Hydrology and Earth System Sciences* (2005).

[76] Zeileis, A., Leisch, F., Hornik, K. & Kleiber, C. strucchange: An R Package for Testing for Structural Change in Linear Regression Models. *Journal of Statistical Software* **7**, 1–38 (2002). URL https://doi.org/10.18637/jss.v007.i02.

[77] Zeileis, A. A Unified Approach to Structural Change Tests Based on ML Scores, F Statistics, and OLS Residuals. *Econometric Reviews* **24**, 445–466 (2005). URL https://doi.org/10.1080/07474930500406053. Publisher: Taylor & Francis _eprint: https://doi.org/10.1080/07474930500406053.

[78] Friedman, J. H. Greedy Function Approximation: A Gradient Boosting Machine. *The Annals of Statistics* **29**, 1189–1232 (2001). URL https://www.jstor.org/stable/2699986. Publisher: Institute of Mathematical Statistics.

[79] Roberts, D. R. *et al.* Cross-validation strategies for data with temporal, spatial, hierarchical, or phylogenetic structure. *Ecography* **40**, 913–929 (2017). URL https://onlinelibrary.wiley.com/doi/abs/10.1111/ecog.02881. _eprint: https://nsojournals.onlinelibrary.wiley.com/doi/pdf/10.1111/ecog.02881.

[80] Saito, T. & Rehmsmeier, M. The Precision-Recall Plot Is More Informative than the ROC Plot When Evaluating Binary Classifiers on Imbalanced Datasets. *PLOS ONE* **10**, e0118432 (2015). URL https://journals.plos.org/plosone/article?id=10.1371/journal.pone.0118432. Publisher: Public Library of Science.

[81] Lundberg, S. M. & Lee, S.-I. A Unified Approach to Interpreting Model Predictions. *NIPS'17: Proceedings of the 31st International Conference on Neural Information Processing Systems* (2017).

[82] Cohen, J. A Coefficient of Agreement for Nominal Scales. *Educational and Psychological Measurement* **20**, 37–46 (1960). URL https://doi.org/10.1177/001316446002000104. Publisher: SAGE Publications Inc.

[83] Light, R. J. Measures of response agreement for qualitative data: Some generalizations and alternatives. *Psychological Bulletin* **76**, 365–377 (1971).

[84] Singer, M. B. *et al.* Hourly potential evapotranspiration at 0.1° resolution for the global land surface from 1981-present. *Scientific Data* **8**, 224 (2021). URL https://www.nature.com/articles/s41597-021-01003-9. Publisher: Nature Publishing Group.

[85] Fan, Y., Li, H. & Miguez-Macho, G. Global Patterns of Groundwater Table Depth. *Science* **339**, 940–943 (2013). URL https://www.science.org/doi/10.1126/science.1229881. Publisher: American Association for the Advancement of Science.

Table of Contents

Table S1 Sensitivity EWS calculation parameters

Table S1. Sensitivity of transpiration, soil moisture, and precipitation EWS signs to analysis configuration for a 50 by 50-pixel tile at 0.25 degrees. Values are Cohen's K (chance-corrected agreement) computed pixel-wise between class-labelled Kendall's τ maps (-1, 0, +1), where | τ | < 0.05 and p > 0.05 are treated as 0. Light's K is the pairwise-average K across all configuration pairs. Columns report the mean K across matched configuration pairs that differ only in sampling frequency (weekly vs monthly), window length (2.5-, 5-, 10-years), first-differencing, or STL robustness choice. Negative values indicate systematic disagreement beyond chance.

Variable	Indicator	Light's K	Frequency only	Window only	Diff. only	STL only
Transpiration	AC1	0.157	0.036	0.417	0.272	0.523
	SD	0.096	-0.111	0.354	0.406	0.329
	Skew	0.067	0.132	0.482	-0.195	0.548
	Kurt	0.106	-0.045	0.289	0.279	0.556
	FD	0.153	-0.080	0.472	0.415	0.240
	Mean	**0.116**	**-0.014**	**0.403**	**0.235**	**0.439**
Soil moisture	AC1	0.174	0.444	0.231	0.156	0.508
	SD	0.558	0.643	0.631	0.705	0.514
	Skew	0.035	0.004	0.391	-0.032	0.171
	Kurt	0.211	0.325	0.422	0.111	0.213
	FD	0.184	0.176	0.760	0.058	0.638
	Mean	**0.233**	**0.318**	**0.487**	**0.200**	**0.409**
Precipitation	AC1	0.206	0.027	0.521	0.369	0.596
	SD	0.291	0.169	0.580	0.433	0.623
	Skew	0.092	0.030	0.526	-0.027	0.432
	Kurt	0.164	0.027	0.483	0.330	0.483
	FD	0.199	0.027	0.497	0.288	0.503
	Mean	**0.190**	**0.056**	**0.521**	**0.278**	**0.527**

Figure S2 Kendall's τ of individual EWS indicators for transpiration

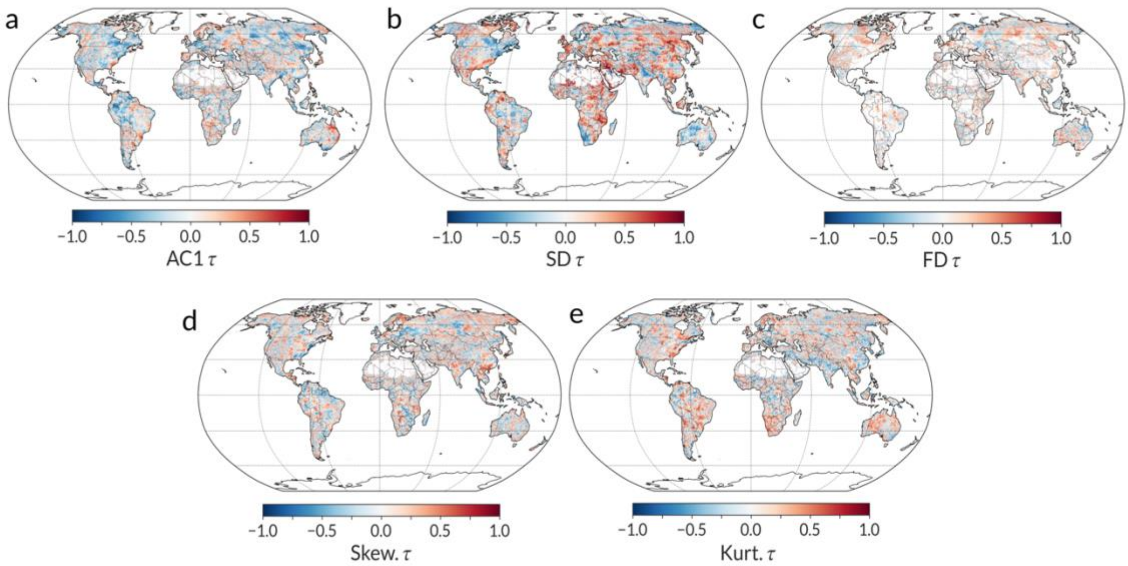

Figure S2a. Transpiration. *Kendall's τ of individual EWS indicators. No significance filtering is applied.*

Figure S2 Kendall's τ of individual EWS indicators for soil moisture

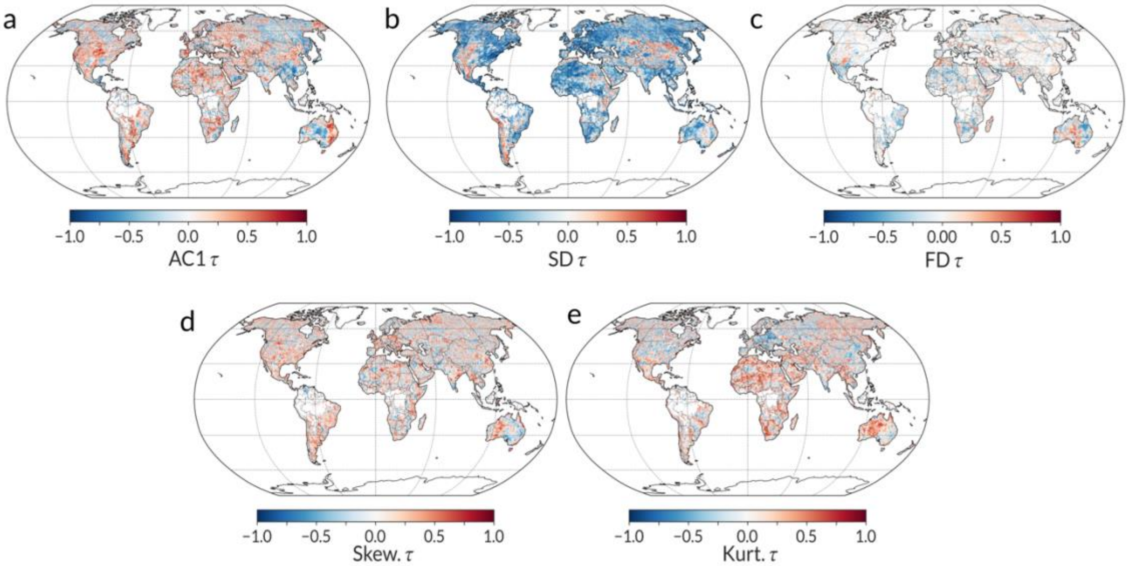

Figure S2b. Soil moisture. *Kendall's τ of individual EWS indicators. No significance filtering is applied.*

Figure S2 Kendall's τ of individual EWS indicators for precipitation

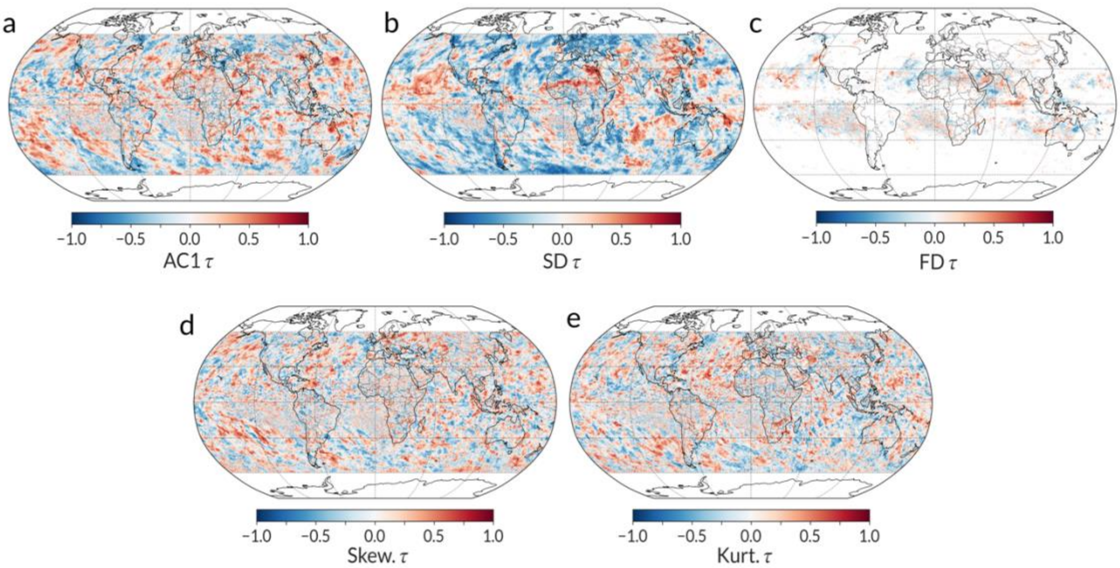

Figure S2c. Precipitation. *Kendall's τ of individual EWS indicators. No significance filtering is applied, and Kendall's τ of ocean pixels are included.*

Figure S3 Delta of individual EWS indicators for transpiration

Here, we calculated the time-ordered difference between the minimum and maximum value of the each of the EWS indicators (δ) over the time series (as per Rocha, 2022), which provides information about the absolute change in indicator value over the time series.

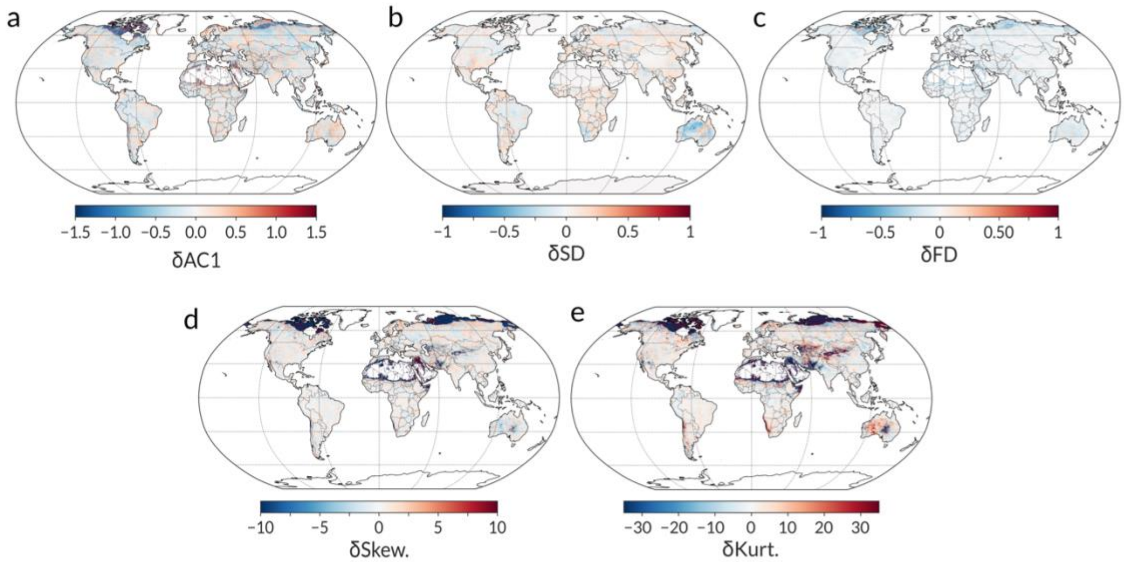

Figure S3a. Transpiration. *Time ordered difference between the minimum and maximum value of the EWS indicators. No significance filtering is applied.*

Figure S3 Delta of individual EWS indicators for soil moisture

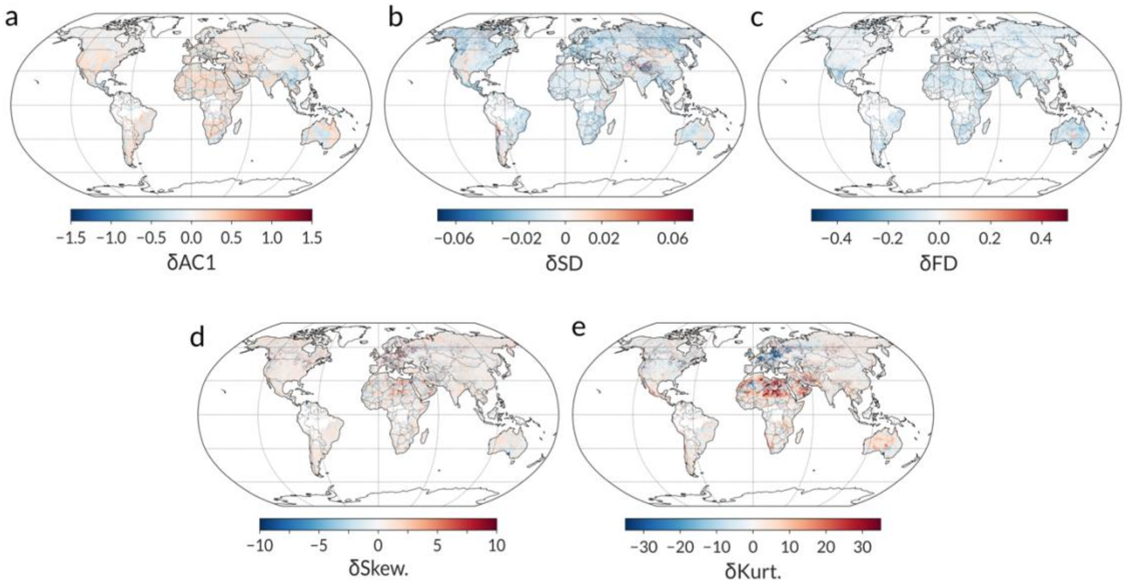

Figure S3b. Soil moisture. *Time ordered difference between the minimum and maximum value of the EWS indicators. No significance filtering is applied.*

Figure S3 Delta of individual EWS indicators for precipitation

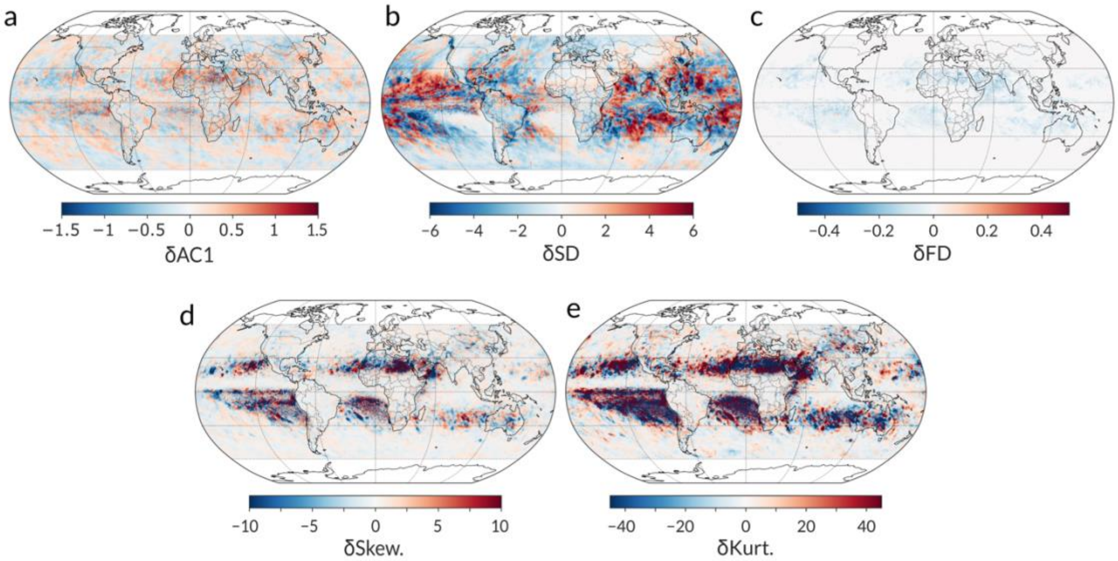

Figure S3c. Precipitation. *Time ordered difference between the minimum and maximum value of the EWS indicators. No significance filtering is applied, and δ of ocean pixels are included.*

Figure S4 Theil-Sen slope of individual EWS indicators for transpiration

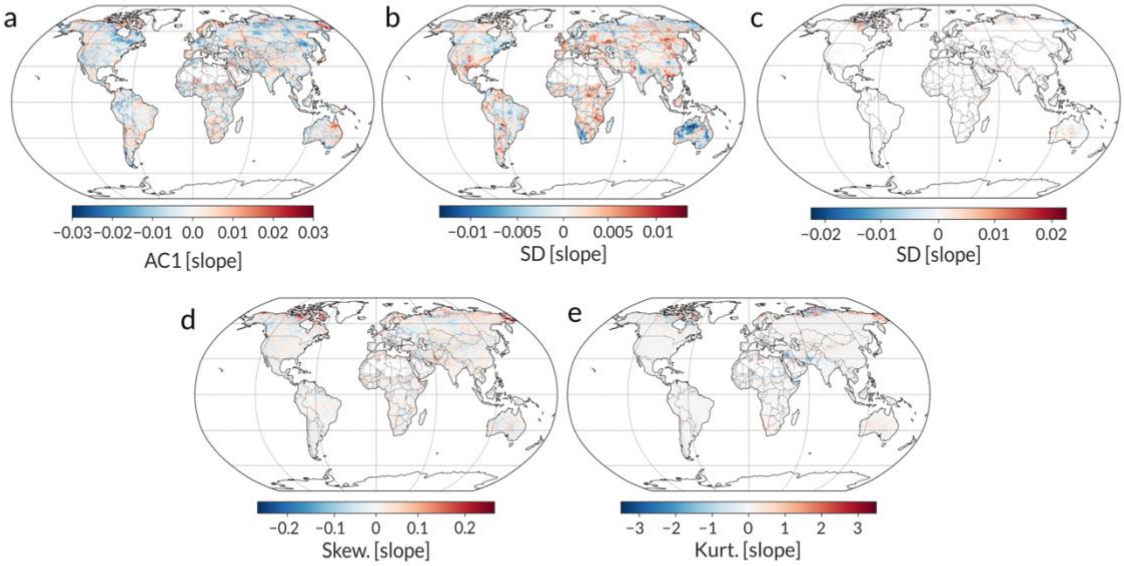

Figure S4a. Transpiration. *Theil-Sen slope of the EWS indicators. No significance filtering is applied.*

Figure S4 Theil-Sen slope of individual EWS indicators for soil moisture

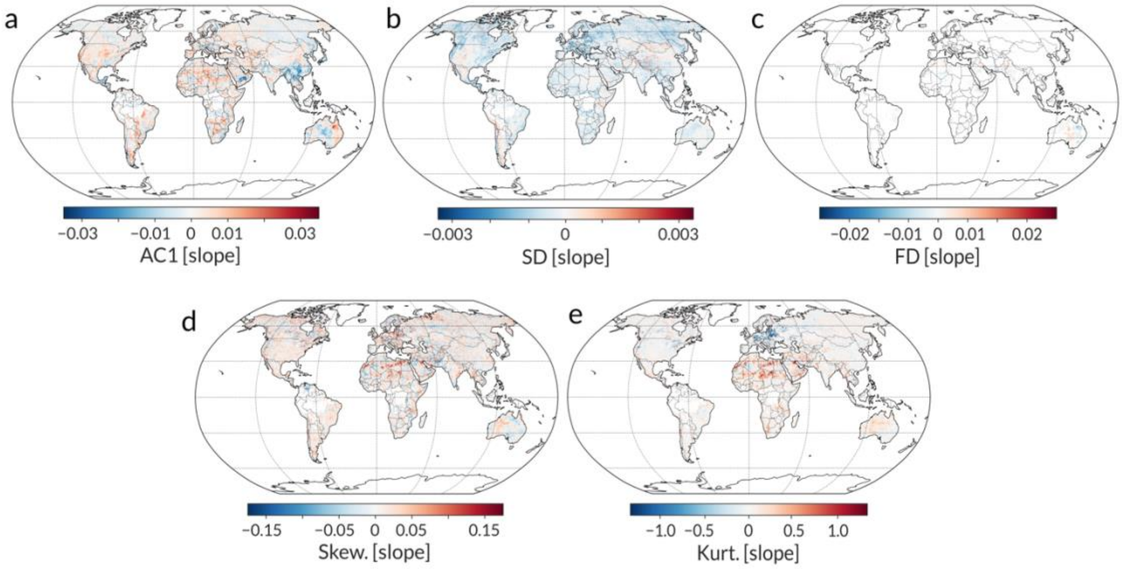

Figure S4b. Soil moisture. *Theil-Sen slope of the EWS indicators. No significance filtering is applied.*

Figure S4 Theil-Sen slope of individual EWS indicators for precipitation

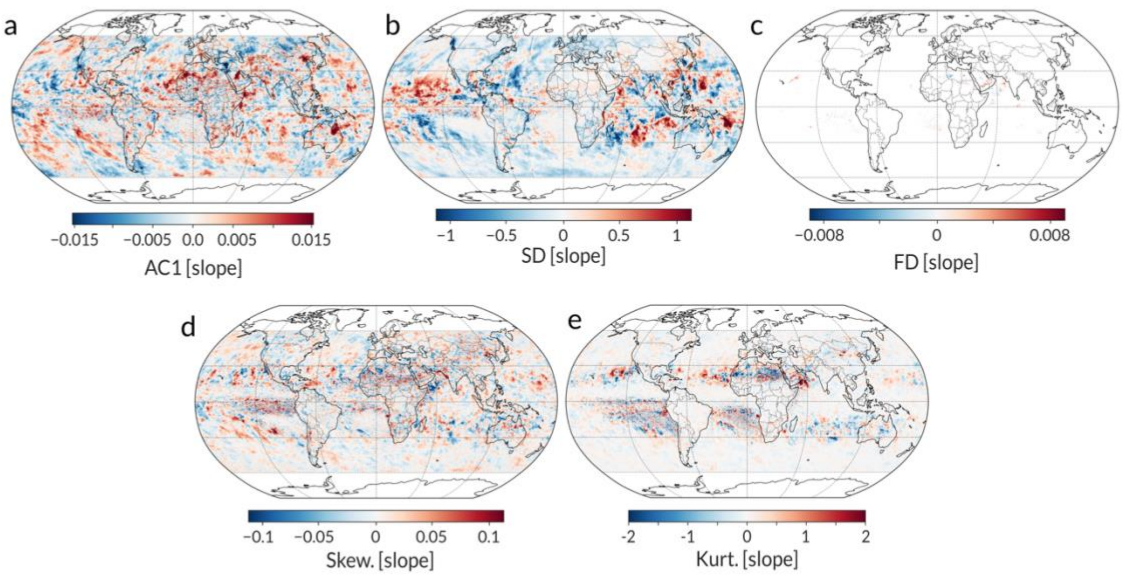

Figure S4c. Precipitation. *Theil-Sen slope of the EWS indicators. No significance filtering is applied, and Theil-Sen slopes of ocean pixels are included.*

Figure S5 Change in mean of individual EWS indicators for transpiration

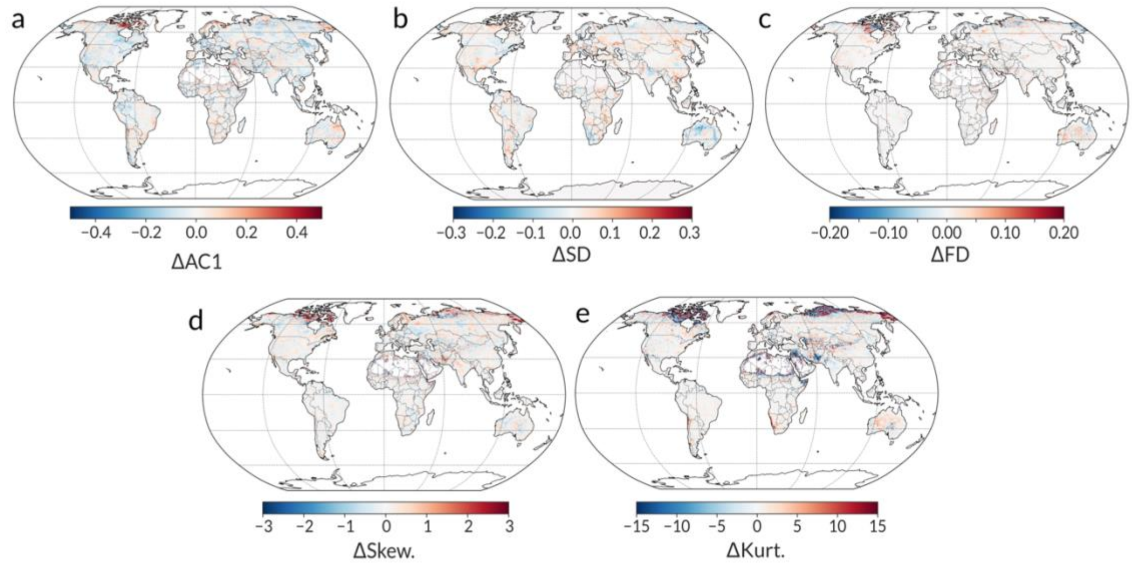

Figure S5a. Transpiration. *Difference between the means of the EWS indicator value in the second half and the first half of the indicator time series.*

Figure S5 Change in mean of individual EWS indicators for soil moisture

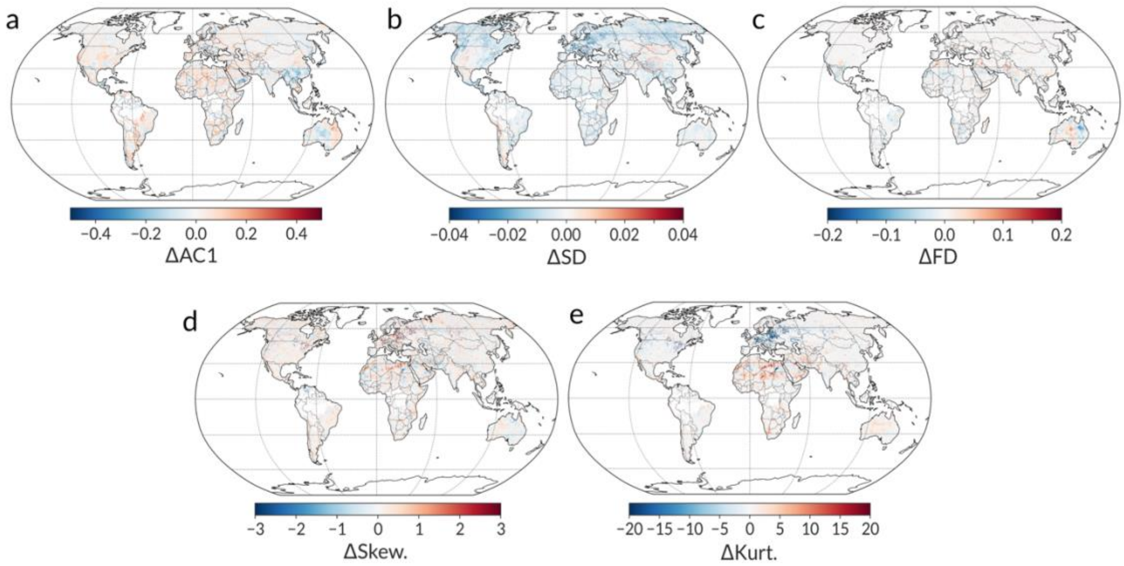

Figure S5b. Soil moisture. *Difference between the means of the EWS indicator value in the second half and the first half of the indicator time series.*

Figure S5 Change in mean of individual EWS indicators for precipitation

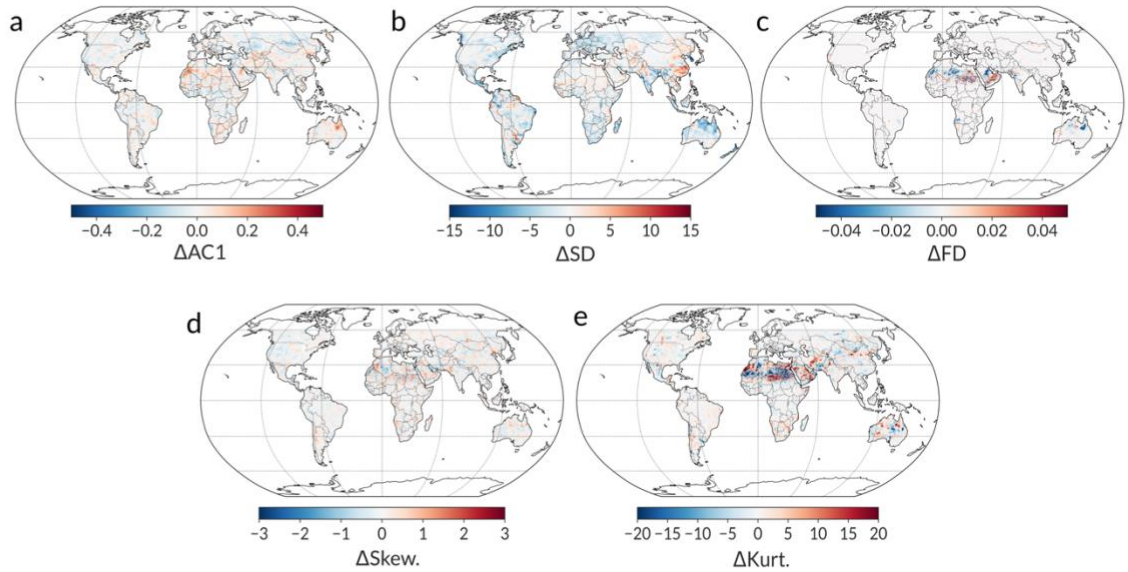

Figure S5c. Precipitation. *Difference between the means of the EWS indicator value in the second half and the first half of the indicator time series.*

Figure S6 Agreement across trend estimation methods

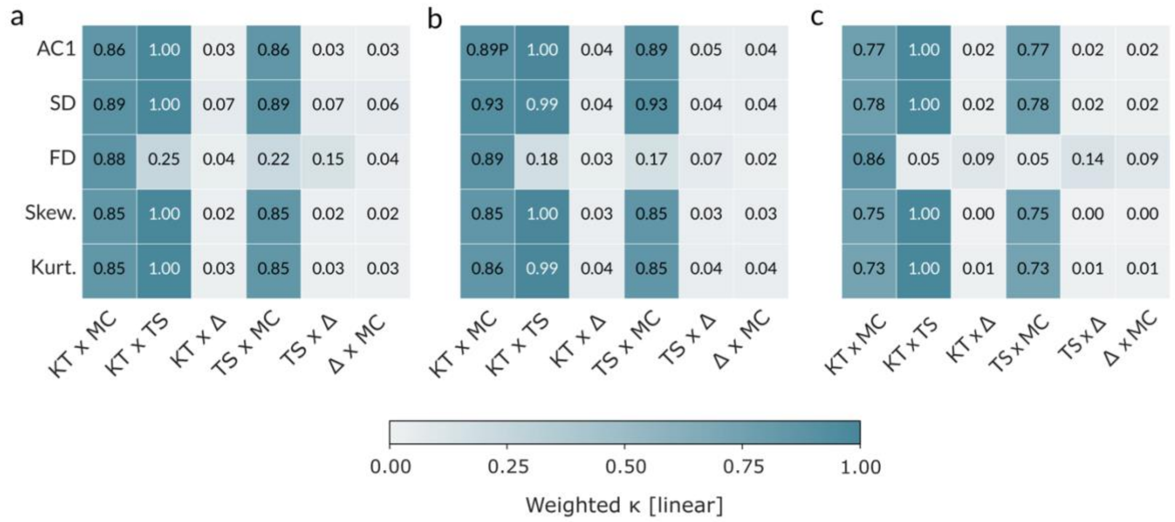

Figure S6. Agreement between methods of trend detection. *Comparison of trend estimation approaches for AC1, SD, FD, Skew., and Kurt. between KT (Kendall-Tau, $p < 0.05$), TS (Theil–Sen slope, $p < 0.05$), Δ (time-ordered difference between maximum and minimum), and MC (mean-change between time series halves, Welch's t-test $p < 0.05$) using all grid cells ($n = 1036800$). Heatmap's report the linear-weighted Cohen's κ across method pairs for each indicator.*

Figure S7 Cumulative land area with detected breakpoints

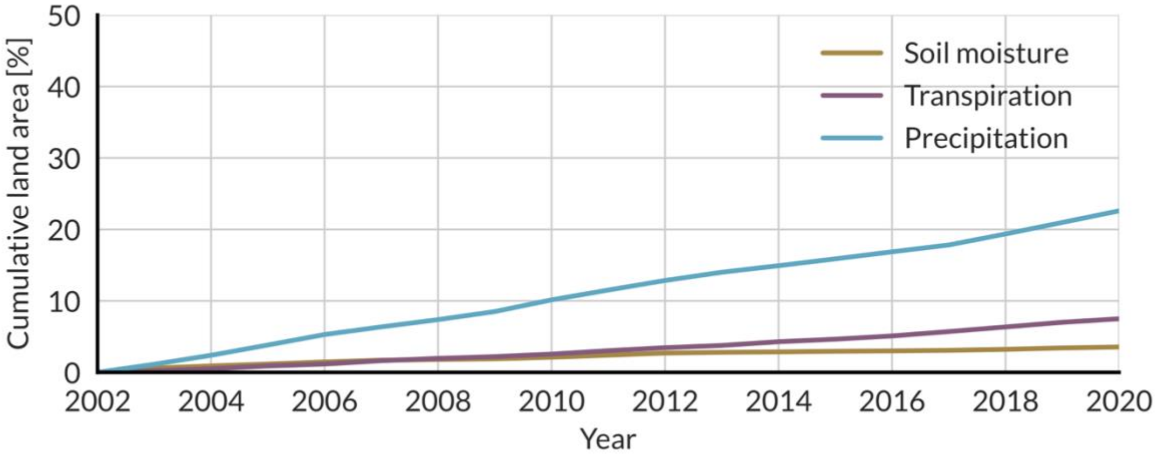

Figure S7. *Cumulative land area with breakpoints detected using the structural change test ($p < 0.05$). The total land area for precipitation is 60°S to 60°N.*

Figure S8 F1 score of abrupt shift detection methods

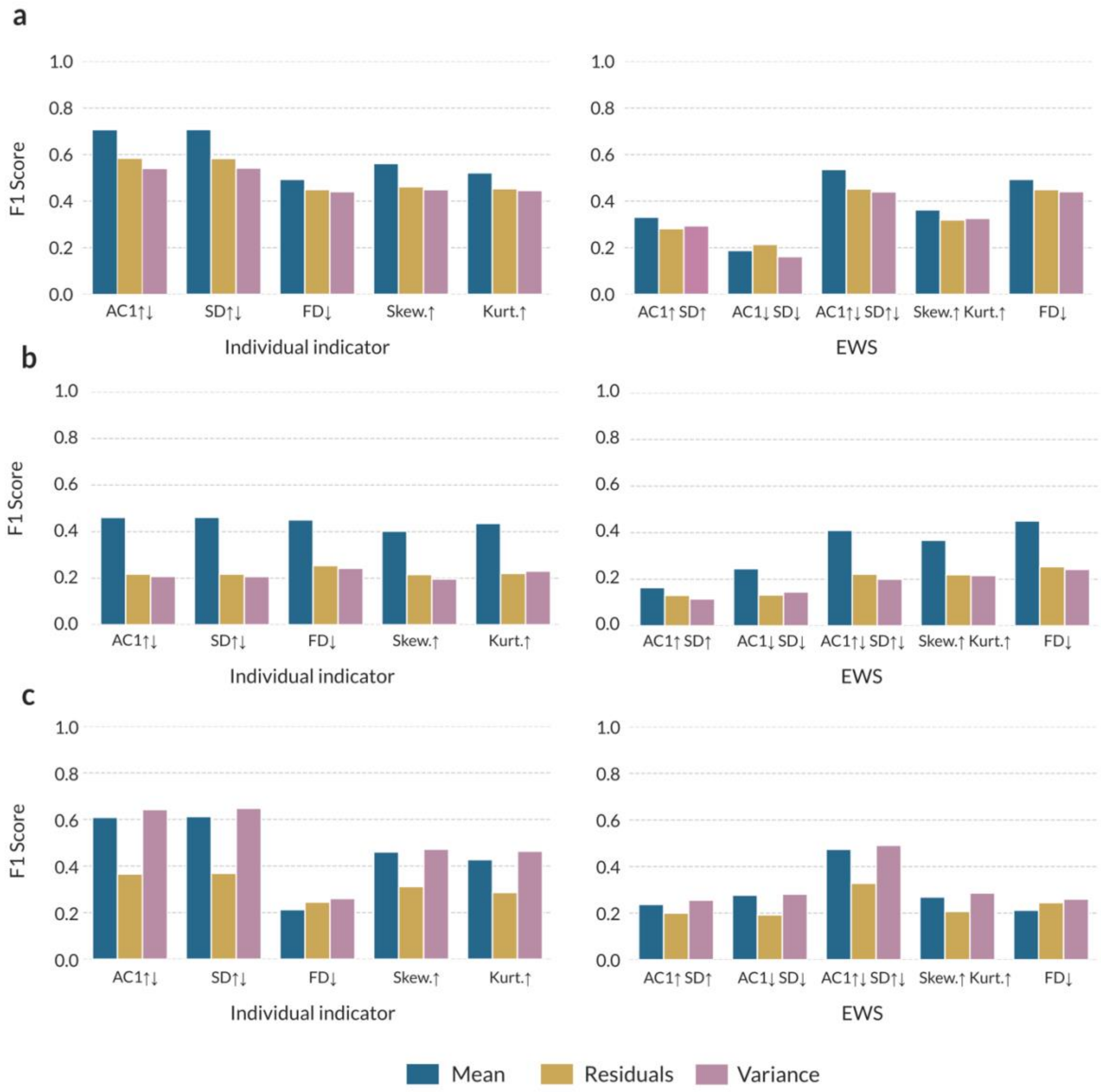

Figure S10. *F1 score of the different abrupt shift methods. Calculated from the confusion matrix that compares Kendall's τ from the full time series of the green water variable to pixels where we detect an abrupt shift, for transpiration (a), soil moisture (b), and precipitation (c). We use the detected breakpoints in residuals as the most conservative test to reduce false positives.*

Table S9 Environmental feature variables included in XGBoost models

Table S9. *Environmental feature variables for XGBoost classification model. The data sources, green water variable for which the features were included, and processing notes are listed.*

Driver	Source	Time	Target	Processing notes
Temperature	ERA5 monthly	2000-2023	P, Et, SM	Calculated mean, SD, and trend of monthly values over time.
Precipitation	ERA5 monthly	2000-2023	P, Et, SM	Calculated mean, SD, and trend of monthly values over time.
Soil moisture	ERA5 monthly	2000-2023	P, Et, SM	Calculated mean, SD, and trend of monthly values over time.
Transpiration	ERA5 Land	2000-2023	P, Et, SM	Calculated mean, SD, and trend of monthly values over time.
Potential evapo-transpiration [Epot]		2000-2023	P, Et, SM	Coarsened to 0.25 degrees, resampled to monthly. Calculated mean, SD, and trend of monthly values over time.
ENSO	NASA	2000-2023	P, Et, SM	Re-indexed ENSO index to precipitation time indices, and calculated the pixel-wise correlation between ENSO and precipitation.
Groundwater table depth [GW]		2000-2023	Et, SM	Coarsened to 0.25 degrees, calculated mean, SD, and trend of monthly values over time.
Boundary layer height	ERA5 Monthly	2000-2023	P, Et, SM	Calculated mean, SD, and trend of monthly values over time.
Convective available potential energy [CAPE]	ERA5 monthly	2000-2023	P, Et, SM	Calculated mean, SD, and trend of monthly values over time.
Gross Primary Productivity [GPP]	MODIS	2014-2023	Et, SM	Calculated mean, SD, and trend of monthly values over time. NaN values (i.e. no vegetation) filled with 0.
Tree cover	ERA5 Land	2000-2023	Et, SM	Calculated mean, SD, and trend of monthly values over time. NaN values (i.e. no vegetation) filled with 0.
Non-tree cover	ERA5 Land	2000-2023	Et, SM	Calculated mean, SD, and trend of monthly values over time. NaN values (i.e. no vegetation) filled with 0.
Irrigated area	FAO	2005	Et, SM	Percentage area equipped for irrigation, NaN values (i.e. no irrigation) filled with 0.

Table S10 Class distribution and model performance

The XGBoost classifier was trained with the following hyperparameters: 300 trees, maximum depth = 8, learning regularization parameters $\lambda = 5$, $\alpha = 0.1$, and subsampling = 0.8). Models were trained on EWS and driver predictors simultaneously. We assess performance was assessed using out-of-fold predictions and cross-validation models, aggregated across folds. We report threshold-agnostic metrics, and use area under the precision–recall curve (PR-AUC) as the primary score, which is able to handle class-imbalance. Fold-specific metrics were summarized by mean and standard deviation.

Table S10. *Class distribution and model performance across folds for XGBoost classifier models for green water variables.*

Variable	N samples	N positives	N folds	Positives per fold	PR AUC [mean ± SD]	ROC AUC [mean ± SD]	Baseline AP	AP increase	Normalised AP increase
Transpiration	234460	1490	5	2981	0.494 ± 0.039	0.903 ± 0.012	0.064	7.719	0.459
Soil moisture	205411	2707	5	541.4	0.215 ± 0.040	0.931 ± 0.008	0.013	16.54	0.205
Precipitation	177810	8241	5	1648.2	0.330 ± 0.042	0.834 ± 0.013	0.046	7.152	0.29

Figure S11 PR and ROC curves of trained XGBoost models

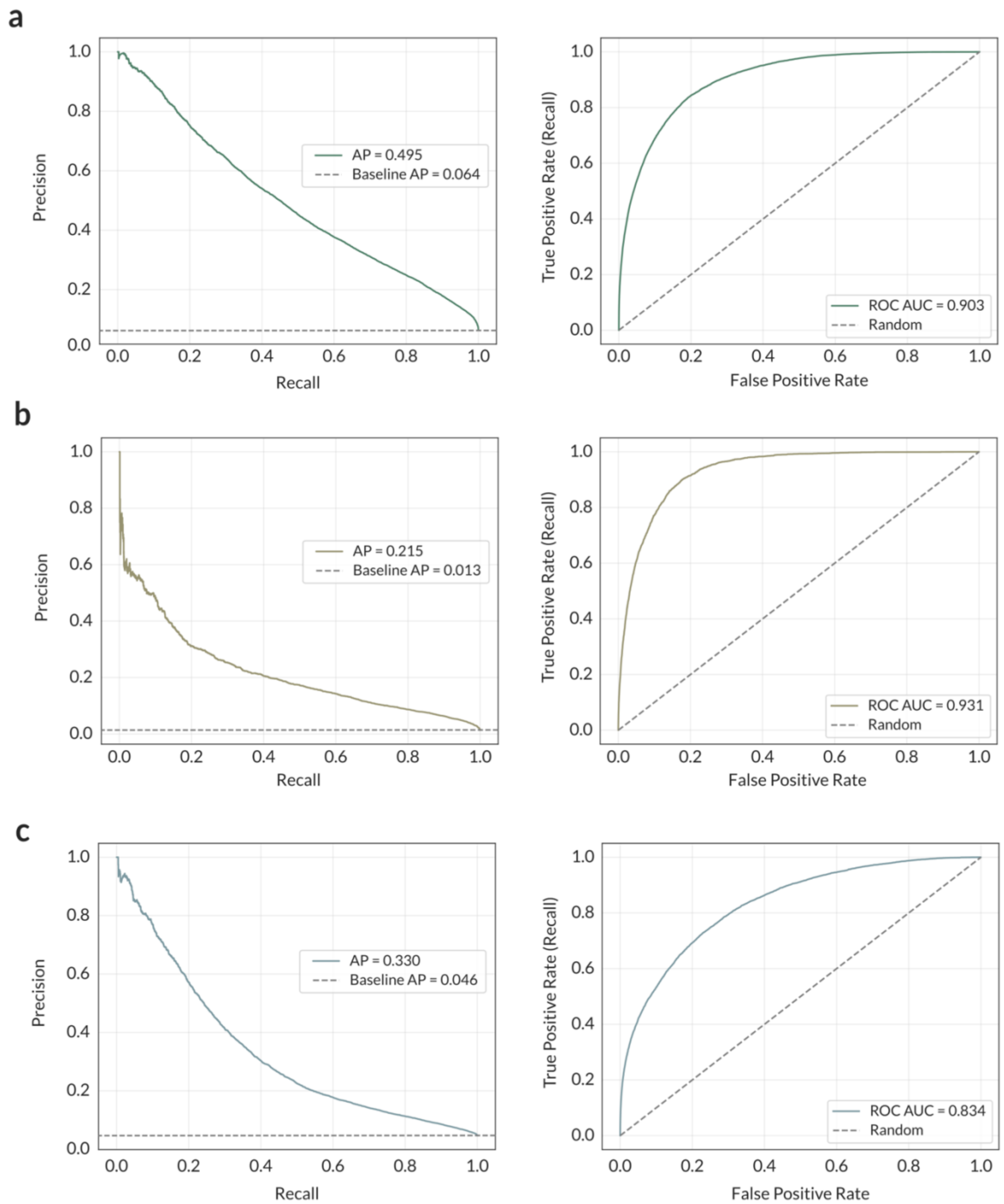

Figure S11. *PR and ROC curves for trained XGBoost models for transpiration (a), soil moisture (b) and precipitation (c), from which performance metrics were calculated.*

Figure S12 Global variable importances

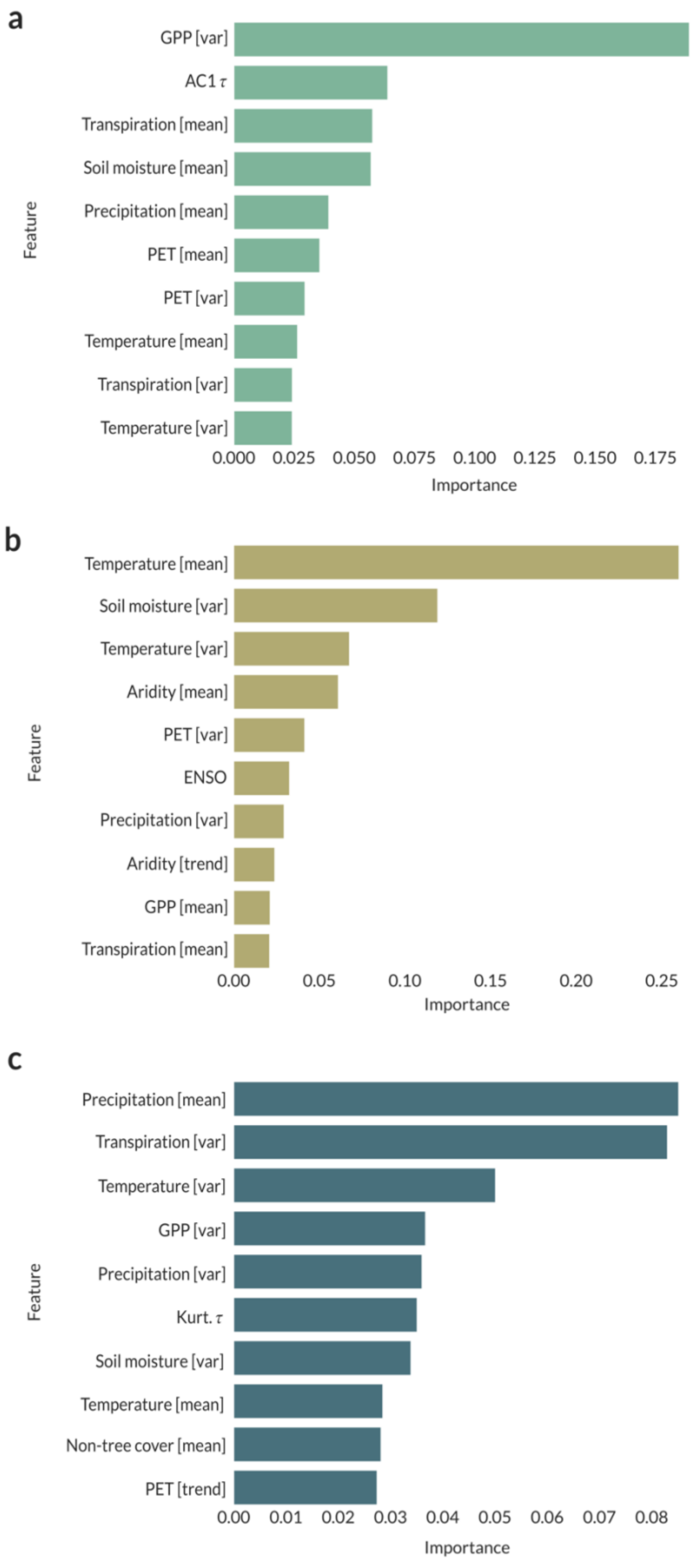

Figure S12. *Global variable importances for transpiration (a), soil moisture (b) and precipitation (c).*

Figure S13 Partial dependence plots of top 5 variables

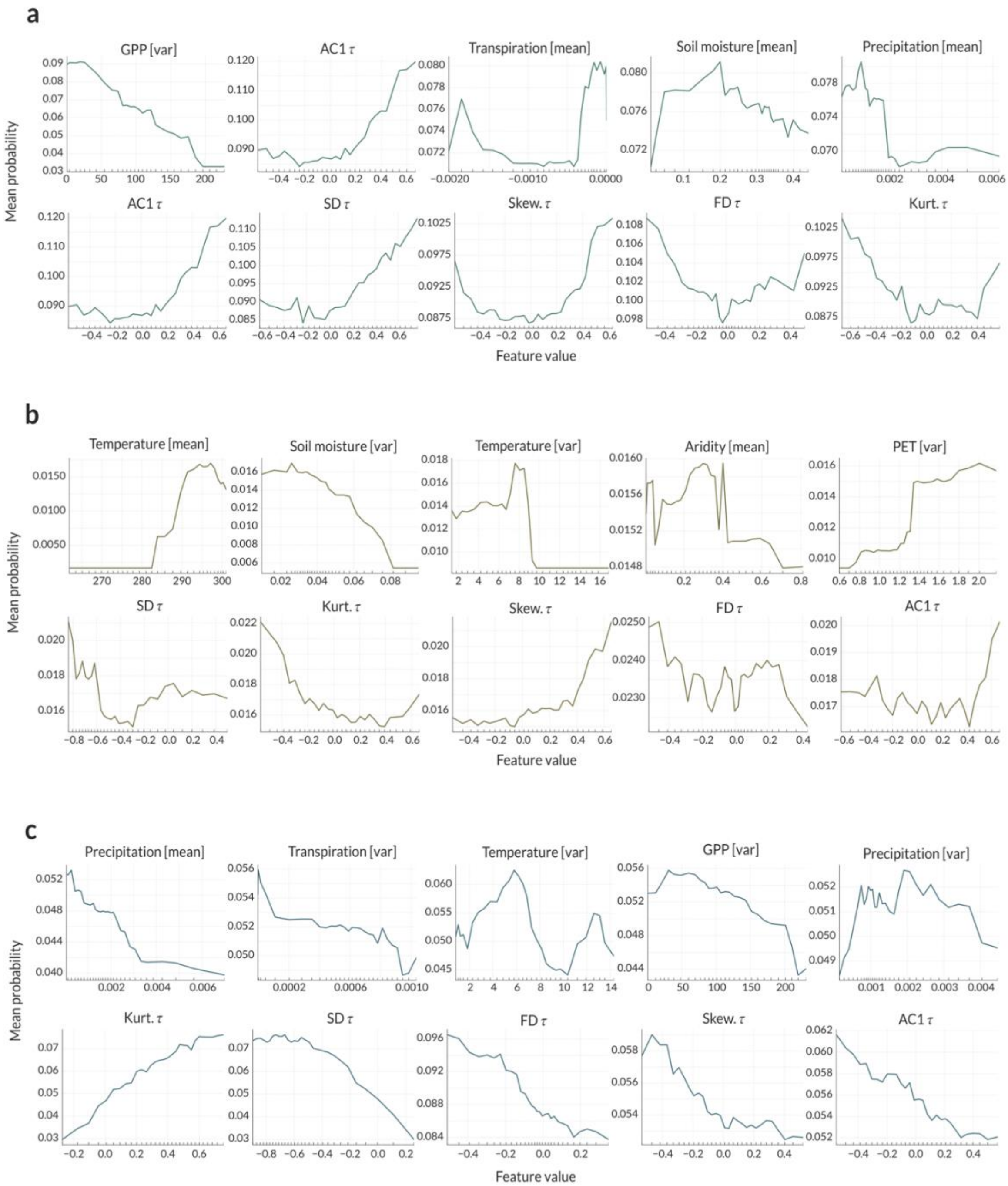

Figure S13. *Partial Dependence Plots for top five variables sorted by variable importance (top panel), and for EWS τ 's, sorted by variable importance (lower panel), for transpiration (a), soil moisture (b) and precipitation (c).*

Figure S14 Biome-resolved absolute SHAP values

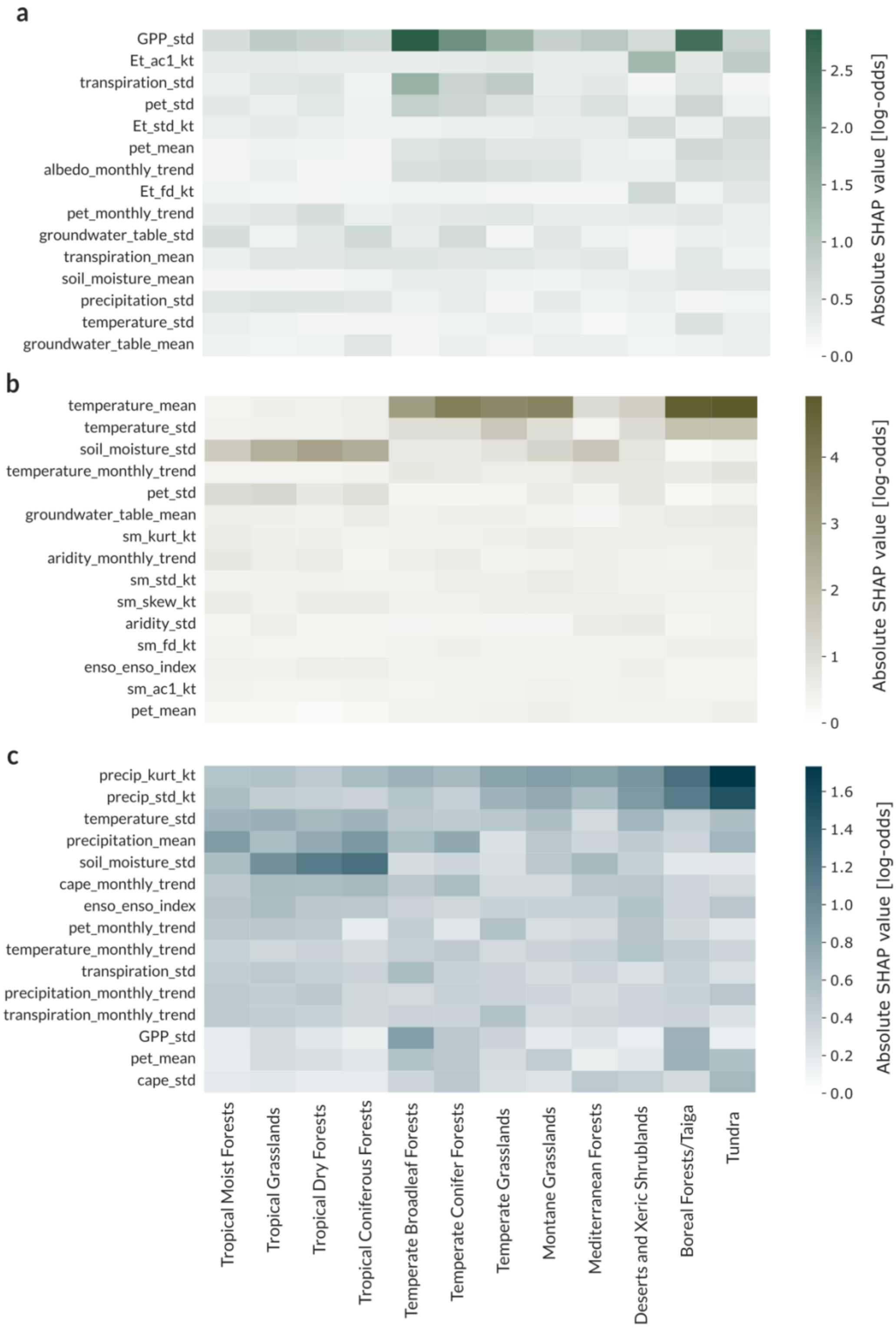

Figure S14. *Biome-resolved absolute SHAP values for transpiration (a), soil moisture (b) and precipitation (c).*